

Multi-Scale Grouped Prototypes for Interpretable Semantic Segmentation

Hugo Porta¹ Emanuele Dalsasso¹ Diego Marcos^{2,3} Devis Tuia¹

¹EPFL ²Inria ³Université Montpellier

{hugo.porta, emanuele.dalsasso, devis.tuia}@epfl.ch
diego.marcos@inria.fr

Abstract

Prototypical part learning is emerging as a promising approach for making semantic segmentation interpretable. The model selects real patches seen during training as prototypes and constructs the dense prediction map based on the similarity between parts of the test image and the prototypes. This improves interpretability since the user can inspect the link between the predicted output and the patterns learned by the model in terms of prototypical information. In this paper, we propose a method for interpretable semantic segmentation that leverages multi-scale image representation for prototypical part learning. First, we introduce a prototype layer that explicitly learns diverse prototypical parts at several scales, leading to multi-scale representations in the prototype activation output. Then, we propose a sparse grouping mechanism that produces multi-scale sparse groups of these scale-specific prototypical parts. This provides a deeper understanding of the interactions between multi-scale object representations while enhancing the interpretability of the segmentation model. The experiments conducted on Pascal VOC, Cityscapes, and ADE20K demonstrate that the proposed method increases model sparsity, improves interpretability over existing prototype-based methods, and narrows the performance gap with the non-interpretable counterpart models. Code is available at github.com/eceo-epfl/ScaleProtoSeg.

1. Introduction

In the last few years, deep learning-based semantic segmentation has seen rapid adoption in numerous fields, from industrial use cases such as autonomous driving [22, 74, 81] to the environmental sciences [5, 48, 65]. This expansion was driven by its increasing performance on a multitude of tasks and benchmarks, often coinciding with an increase in model complexity [11, 64, 86, 89]. This favors un-interpretable black-box models, to the detriment of their explainability.

The models' lack of interpretability is particularly harmful in high-stakes applications [68, 82] and sometimes pre-

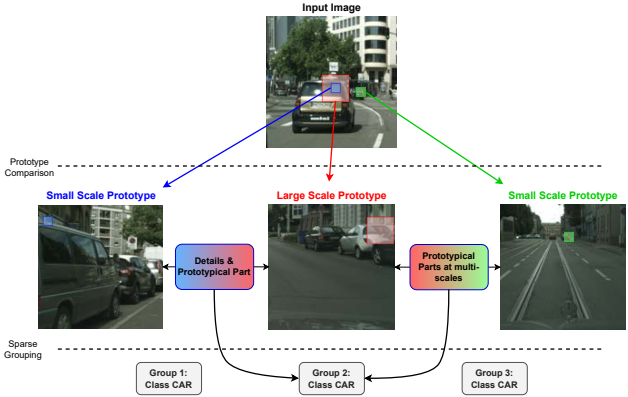


Figure 1. ScaleProtoSeg learns scale-specific prototypes at multiple scales and a sparse prototype grouping to extract patterns referring to different levels of details or scales.

vents the wider adoption of deep learning models in applied fields involving high-stakes decision making [26, 63, 76]. Indeed, deep learning models can rely on spurious cues, such as Clever-Hans predictors, often symptoms of data contamination [2, 49]. This is detrimental in real use cases due to the potential lack of generalization and opaqueness of the decision process. Issues in the generalization of deep learning models are also illustrated by adversarial examples, which can be engineered via small, imperceptible perturbations of images [47] or be inherent in natural images [34].

The field of eXplainable Artificial Intelligence (XAI) aims at alleviating the risks associated with the lack of model interpretability by presenting some aspects of the models' decision process into a form understandable to humans [20]. To produce explainable results, the model design often requires some simplifications that reduce the performance of the original, more complex black-box counterpart [53]. Most methods focus on classification and regression tasks [3, 27, 44, 46, 72], including prototype-based approaches [8]. A few works aim at making semantic segmentation models interpretable [35, 70, 71, 83]. However, no approach considers questions about the relationship between prototypes across semantic classes and scales, despite instances of objects appearing at different positions in the

image or at multiple range of distances. Accounting for these redundancies allows for learning more diverse prototypes for a given object across scales, in turn leading to more explicit interpretability [57].

In this paper, we tackle these gaps and propose a method for multi-scale interpretable semantic segmentation, ScaleProtoSeg (see Figure 1), that (i) explicitly learns prototypes at several scales and (ii) groups the scale-specific prototypes thanks to a sparse grouping mechanism that provides information on the interaction between prototypical parts at multiple scales, while reducing the number of active prototypes contributing to the decision. Multi-scale prototype learning disentangles the information at different scales so that the model and the users have access to different levels of contextual information in the interpretable decision process. The sparse grouping mechanism allows a transparent understanding of the interaction of scale-specific representations such as object details and parts or similar parts at multi-scale (see Figure 1), while maintaining parts correspondences via regularization, avoiding altogether prototype pruning. We are the first to jointly leverage multi-scale representation and prototype learning in an interpretable semantic segmentation model.

We test our methods on three semantic segmentation benchmarks: Pascal VOC 2012 [21], Cityscapes [14], and ADE20K [100], by considering DeepLabv2 [9] as our base model architecture. We first show that multi-scale prototype learning improves the performance of single-scale prototype-based interpretable semantic segmentation methods (with similar amounts of prototypes) across all considered benchmarks. Moreover, thanks to the sparse grouping mechanism, we demonstrate that constraining the decision process to a small group of prototypes per class enforces interpretability while retaining competitive performance. The contributions of our paper can be summarized as follows:

- we propose a multi-scale prototype layer that enforces the model to focus on the prototypical parts’ representations at multiple scales;
- we define a grouping procedure that learns sparse combinations of the scale-specific prototypes across all scales and increases the interpretability of the decision process;
- not only we show the superiority of our ScaleProtoSeg method in three popular datasets in semantic segmentation over the prototype-based method [70], but also highlight its improved interpretability measured in terms of *stability*, *consistency* and *sparsity*.

2. Related works

Semantic segmentation. Fully Convolutional Networks (FCN) [55] are widely used in semantic segmentation meth-

ods. They are based on an encoder-decoder architecture, where the encoder extracts discriminative features from the input image and the decoder converts the learned semantic representation into per-pixel predictions. Following FCN, researchers focused on improving different aspects of the semantic segmentation methods such as enlarging the model receptive field while limiting the parameters increase [10, 94, 96], specifying boundary information [17, 78, 93], or providing contextual information [32, 52, 95]. Some methods proposed specific modules learning pixel affinities or attention [23, 38, 54, 97] to allow the network to base its prediction also on similar pixels that do not lie in the direct vicinity of the pixel at hand. Furthermore, there has been a growing interest in how multi-scale information could be extracted. A common pattern in decoder architectures is the concatenation of scale-specific feature maps at multiple scales [64, 67, 89]. For instance, Chen et al. [9] introduce atrous spatial pyramid pooling (ASPP) to learn in parallel a multi-scale representation from a single-scale feature map. We focus on providing an interpretable version of this model relying on its widely employed decoder multi-scale architecture.

Explainable artificial intelligence. XAI methods can be split into *post-hoc* vs *by-design* approaches. Post-hoc methods aim to explain black-box models after training by using an auxiliary method to generate explanations, while *by-design* approaches enforce interpretability in the model itself. Our proposed method falls into the latter category. Some examples of interpretable *by-design* approaches are concept bottleneck models [43, 46, 57, 62]; attention modules [66, 73, 98, 99] which point to critical parts of each input sample; generalized additive models [3, 31]; and prototype learning introduced in [8, 51], where part of an encoded input image is compared to a set of class-specific prototypes, represented by training samples. Several extensions followed the original paper [8], aiming at enforcing orthogonality in the prototype construction [19, 84], reducing the number of prototypes [69], or even leveraging label taxonomy via a hierarchical structure [30]. Prototype learning can be extended to other tasks beyond image classification such as sequence learning [60] and time series analysis [25] and, most recently, semantic segmentation [70]. In this work, we rely on prototype learning for interpretable semantic segmentation.

Interpretable semantic segmentation. Among the few existing methods tackling this problem, post-hoc approaches extending Grad-CAM to semantic segmentation have been explored [35, 83]. By-design approaches can provide explainable results by leveraging symbolic language [71], through the use of a semantic bottleneck [56] or by exploiting the attention mechanism [28]. Pro-

totypical parts learning was proposed recently in ProtoSeg [70] for interpretable semantic segmentation, extending the classification-based method proposed in [8]. In this work, we aim to investigate multi-scale prototype learning to break the performance/interpretability trade-off present in ProtoSeg. This is achieved by explicitly leveraging the multi-scale nature of semantic segmentation representations (via scale-specific prototypes) and by encouraging sparsity (via sparse grouping across prototypes and scales).

Prototypes and semantic segmentation. Prototype learning based on parametric or non-parametric prototypes has seen an increase of interest in image classification [59, 92], few-shot and zero-shot [42, 75, 90], unsupervised [88] and self-supervised learning [50]. For semantic segmentation, parametric prototypes are used to represent unique class embeddings, both in an explicit [12, 40, 77] or implicit way [101]. Non-parametric prototypes were also leveraged, first in the few-shot learning context [18, 85] and then in more classic semantic segmentation models [39, 87, 101]. The methods in [87, 101] are the closest to our proposition: both compute multiple class-specific prototypes via online clustering and leverage metric learning losses to enforce a compact embedding space. The pixel-wise classification is then performed via nearest-prototype assignment. Despite those similarities, those works compute prototypes in the final embedding space, while we focus on enhanced interpretability via i) prototypical parts through specific regularization and ii) multi-scale object representation. These core differences limit the applicability of direct performance comparisons. Finally, [79, 80] leverage non-parametric prototypes for modality and domain alignment for multi-modal semantic segmentation (e.g. video and point clouds), but do not explore issues related to interpretability or multi-scale prototype learning as our proposed method.

3. Method

In this section, we present our multi-scale grouped prototypes method for interpretable semantic segmentation: ScaleProtoSeg (Figure 2). We first introduce the multi-scale prototype architecture (Section 3.1). Then we describe the proposed grouping mechanism to extract sparse groups of prototypes across scales (Section 3.2). Lastly, we detail the multi-stage training procedure used to learn both prototypes and groups (Section 3.3).

3.1. Multi-scale prototype learning

Our model architecture for multi-scale prototype learning is presented in Figure 2: **Stage 1**. It is composed of a backbone network f , a multi-scale prototype layer g_{proto} , and a linear layer h_{proto} . For an input RGB image $\mathbf{x} \in \mathbb{R}^{H \times W \times 3}$, f outputs a multi-scale feature map

$f(\mathbf{x}) \in \mathbb{R}^{H_r \times W_r \times S \times d}$, representing scale-specific features at S scales, each one with d dimensions. The scalar r is a size reduction factor. In practice, we modify the ASPP layer from [9] to concatenate the scale-specific feature maps instead of summing them. At each scale $s \in \mathcal{S}$, let $\mathbf{z}_s \in \mathbb{R}^d$ be a vector from the scale-specific feature map $f_s(\mathbf{x})$. As illustrated in Figure 2, this vector represents the features extracted from an area of the input image corresponding to the receptive field at scale s . The multi-scale prototype layer g_{proto} is composed of M learnable scale-dependent prototypes, where the m^{th} scale-dependent prototype (with $m \in [1, \dots, M]$) is described by the vector $\mathbf{p}_{s,m} \in \mathbb{R}^d$, which is randomly initialized and learned through gradient descent. For each feature vector \mathbf{z}_s , the prototypes' activations are computed following ProtoPNet [8]:

$$g_{\text{proto}}(\mathbf{z}_s, \mathbf{p}_{s,m}) = \log \left(\frac{\|\mathbf{z}_s - \mathbf{p}_{s,m}\|_2^2 + 1}{\|\mathbf{z}_s - \mathbf{p}_{s,m}\|_2^2 + \epsilon} \right) \quad (1)$$

with $\epsilon \ll 1$ a constant for numerical stability. Then, for each scale-specific feature vector \mathbf{z}_s , the M activation scores $[g_{\text{proto}}(\mathbf{z}_s, \mathbf{p}_{s,1}), \dots, g_{\text{proto}}(\mathbf{z}_s, \mathbf{p}_{s,M})]$ are concatenated across the S scales indexed by s . The linear layer h_{proto} , with weight matrix $\mathbf{w}_{h_{\text{proto}}} \in \mathbb{R}^{C \times M \cdot S}$, learns a mapping from those prototype activations to the C output classes probabilities. The classification probabilities map, obtained after processing all feature vectors $\mathbf{z} = [\mathbf{z}_1, \dots, \mathbf{z}_S]$ in parallel, is of dimension $H_r \times W_r \times C$. To upscale it to the original image resolution and produce the final segmentation map, the classification probability is linearly interpolated.

For semantic segmentation, the objective is to learn prototypes that are assigned to a specific class $c \in \mathcal{C}$. This is enforced by initializing the weights $\mathbf{w}_{h_{\text{proto}}}$ of the linear layer h_{proto} following [8], and replicating the same assignment to a specific class across all scales, such as with:

$$w_{h_{\text{proto}}}^{(c,m)} = \begin{cases} 1 & \text{if } \mathbf{p}_{s,m} \in P_c \\ -0.5 & \text{otherwise} \end{cases}$$

where P_c is the set of prototypes that we assign to class $c \in \mathcal{C}$, across all scales and $m \in [1, \dots, |P_c|]$. Those weights are frozen for the majority of the training procedure (see Section 3.3) to maintain the steering of the prototypes toward class-specific patterns.

3.2. Prototype grouping

Our model architecture for prototype grouping is presented in Figure 2: **Stage 2**. Once the scale-specific prototypes $\mathbf{p}_{s,m}$ are learned through the multi-scale learning stage as described in Section 3.1, we group them into sparse groups across scales. For this purpose, we use class-specific grouping functions: $g_c(\mathbf{z}) = g_{\text{group}}^c(g_{\text{proto}}(\mathbf{z}, P_c))$, which group prototypes assigned to the same class and compute

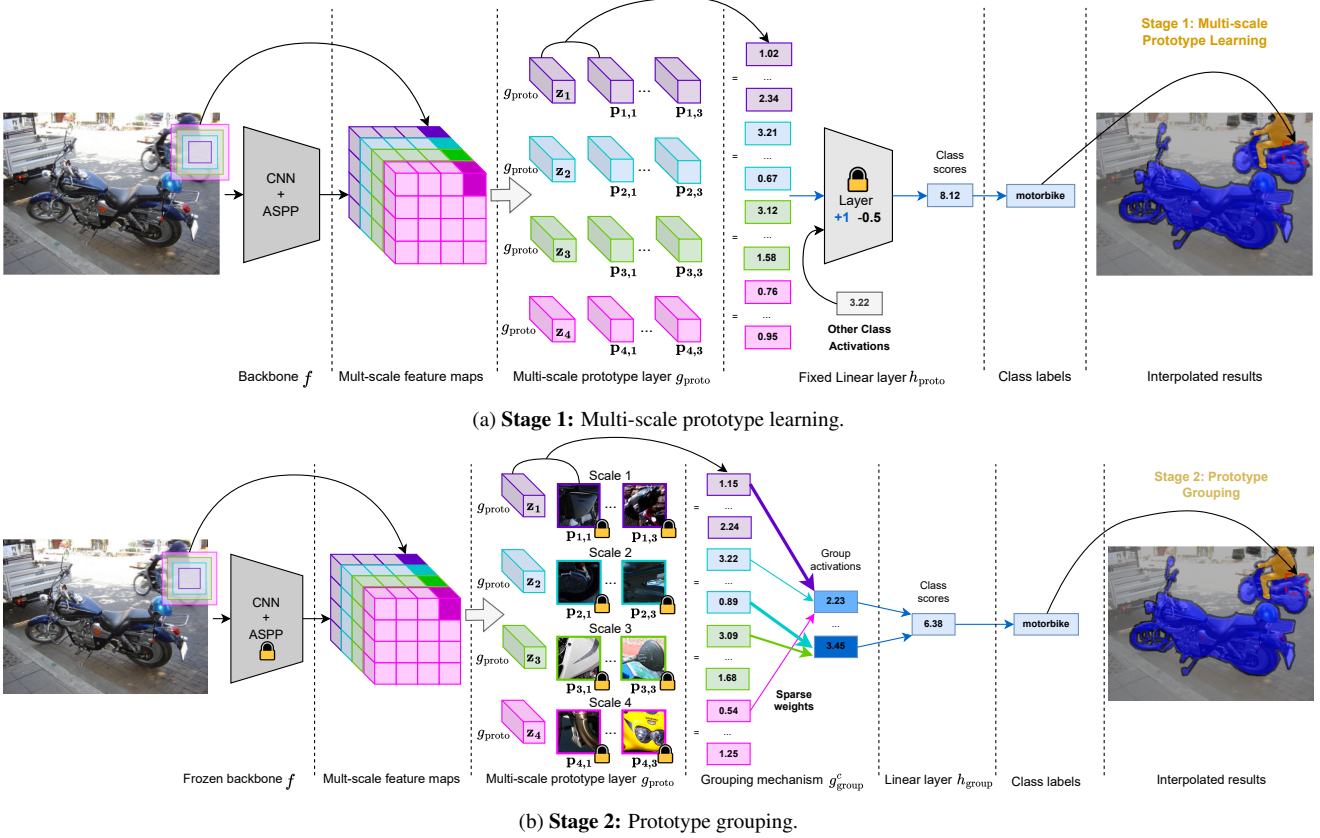


Figure 2. Overall architecture of ScaleProtoSeg. Each color in the feature maps and following layers corresponds to a specific scale ($S = 4$ and $M = 3$ in this illustration).

the groups' activations $g_c(\mathbf{z}) \in \mathbb{R}^{N_c}$, where N_c is the number of groups per class. Following [57], those functions are parametrized by sparse non-negative weight matrices $\mathbf{w}_{g,c} \in [0, 1]^{N_c \times |P_c|}$, where each row is constrained on the probability simplex: $w_{g,c}^{(n,m)} \geq 0$ and $\sum_m w_{g,c}^{(n,m)} = 1, \forall n \in [1, \dots, N_c]$. The output group activation for the group $g_{c,n}(\mathbf{z})$ that combines the prototypes $\mathbf{p}_m \in P_c$ at multiple scales is computed as follows:

$$g_{c,n}(\mathbf{z}) = \prod_{m=1, \dots, |P_c|} g_{\text{proto}}(\mathbf{z}, \mathbf{p}_m)^{w_{g,c}^{(n,m)}}. \quad (2)$$

The projection on the simplex and the weighted geometric mean are used to learn sparse weight matrices, as group activations can be high only if all prototypes in the group are strongly activated. The linear layer h_{group} is adapted to accommodate groups through a weight matrix $\mathbf{w}_{h_{\text{group}}} \in \mathbb{R}^{C \times N}$, where $N = N_c \times C$ is the total number of groups, each one containing a sparse combination of the set of $M \times S$ prototypes. The layer h_{group} follows the same initialization process as in Section 3.1, but with group assignment.

3.3. Multi-stage training procedure

In order to train ScaleProtoSeg, we resort to a two-stage training procedure: first, we learn the multi-scale prototypes and project them to the training set patches, without any grouping. Then we learn the prototypes grouping functions with the prototypes fixed. The two stages are illustrated in Figure 2 and detailed below.

Stage 1: Multi-scale prototype learning. For the multi-scale prototype learning we apply a training procedure similar to [8, 70], which consists of three steps. First, in a warm-up step, the ASPP [9] and the scale-specific prototypes are trained while freezing the rest of the backbone f and the last linear layer h_{proto} . Second, we run a joint optimization stage where all the model is trained except the last linear layer h_{proto} . Third, for all scales $s \in \mathcal{S}$, the prototypes are projected to their nearest vector \mathbf{z}_s from the training set, and duplicates are removed. The fine-tuning stage from [70] is not necessary for ScaleProtoSeg, as we replace the last layer h_{proto} with h_{group} in the second stage below. Moreover, contrary to [8, 70], we do not need to run their pruning algorithm, as the sparse grouping mechanism will also enforce a natural decrease in the number of prototypes used.

In all those steps, we apply as a regularization loss the diversity loss [70], which aims to prevent the prototypes from activating the same region of an object. To enforce diversity among scale-specific prototypes, the diversity loss is evaluated independently at each scale $s \in \mathcal{S}$. Indeed, the multi-scale prototype layer aims to represent similar parts across scales with different contextual information. For each class $c \in \mathcal{C}$ and scale $s \in \mathcal{S}$, we note $P_{s,c}$ as the set of prototypes assigned to c and s . Furthermore, for the scale-specific feature map $f_s(\mathbf{x})$ we note $y_{\mathbf{z}} \in \{1, \dots, C\}$ as the ground truth labels for each vector \mathbf{z} across all scales.

First, for the diversity loss, we define $v(f_s(\mathbf{x}), \mathbf{p}_{s,m})$ as the softmax vector of distances between each vector assigned to a class c , and a prototype $\mathbf{p}_{s,m} \in P_{s,c}$:

$$v(f_s(\mathbf{x}), \mathbf{p}_{s,m}) = \text{softmax}(\|\mathbf{z}_s - \mathbf{p}_{s,m}\|^2 : \forall \mathbf{z}_s \in f_s(\mathbf{x}), y_{\mathbf{z}} = c) \quad (3)$$

Next we use the Jeffrey similarity $S_J(U_1, \dots, U_l)$ as a measure of similarity between distributions (U_1, \dots, U_l) , following ProtoSeg [70]:

$$S_J(U_1, \dots, U_l) = \frac{1}{\binom{l}{2}} \sum_{i < j} \exp(-D_J(U_i, U_j)) \quad (4)$$

with $D_J(U, V)$ the Jeffrey’s divergence defined in [41]. The diversity loss is then computed as follows for a given class c and scale s :

$$L_J(f_s(\mathbf{x}), P_{s,c}) = S_J(v(f_s(\mathbf{x}), \mathbf{p}_{s,1}), \dots, v(f_s(\mathbf{x}), \mathbf{p}_{s,M})) \quad (5)$$

and the total loss across all classes and scales is:

$$L_J = \frac{1}{C \cdot S} \sum_{c \in \mathcal{C}} \sum_{s \in \mathcal{S}} L_J(f_s(\mathbf{x}), P_{s,c}) \quad (6)$$

The final loss term for the multi-scale prototype learning (**Stage 1**) becomes:

$$L_{\text{proto}} = L_{\text{CE}} + \lambda_J \cdot L_J \quad (7)$$

with L_{CE} the per patch cross-entropy loss and λ_J a hyperparameter controlling the weight of the regularization.

Stage 2: Prototype grouping mechanism. The multi-scale prototype grouping mechanism is applied to the learned scale-specific prototypes after they are projected to the training set patches. We proceed with two steps: we first run a warm-up step to train the class-specific grouping functions g_{group}^c while keeping the rest of the model frozen, namely the backbone f and the prototypes, so that we maintain interpretability. Then, in the second step, we run a joint training phase where we finetune both the grouping functions and the last linear layer h_{group} . During the learning

of the groups, we apply a sparsity regularization term promoting that only a limited subset of prototypes are active for a given group. For this purpose, we define an entropic loss term, L_{ent} , on the weight matrices $\mathbf{w}_{g,c} \in [0, 1]^{N \times |P_c|}$. Indeed, as we are projecting each row of those weight matrices $\mathbf{w}_{g,c}^{(n,:)}$ on the probability simplex it is possible to directly compute and minimize information theory measures such as the entropy of those rows, to enforce a sparse combination of prototypes among each group. The entropy loss is computed as follows:

$$L_{\text{ent}} = \frac{1}{C \cdot N} \sum_{c \in \mathcal{C}} \sum_{n=1}^{N_c} \sum_{m=1}^M -w_{g,c}^{(n,m)} \log(w_{g,c}^{(n,m)}) \quad (8)$$

Then, in the second step, we fine-tune also the linear layer h_{group} . To enforce more sparsity, following the training protocol from [8], we apply an L1-norm loss term on h_{group} solely on the weights $w_{h_{\text{group}}}^{c,n}$ where the group g_n is not in the set of groups G_c assigned to class c . The total loss term for the grouping mechanism (Figure 2: **Stage 2**) becomes:

$$L_{\text{proto}} = L_{\text{CE}} + \lambda_{\text{ent}} \cdot L_{\text{ent}} + \lambda_{\text{L1}} \cdot \sum_{c \in \mathcal{C}} \sum_{n: g_n \notin G_c} |w_{h_{\text{group}}}^{(c,n)}| \quad (9)$$

where λ_{ent} and λ_{L1} are hyperparameters controlling the weight of the regularization terms. Once the whole architecture is trained, a final post-processing stage is done: the weights of the grouping function matrices $\mathbf{w}_{g,c}$ below a certain threshold α are set to 0. This enforces even more sparsity within the groups.

4. Experiments

4.1. Experimental setup

In all the experiments presented in the section 4.2, we use DeepLabv2 [9] with ResNet-101 [33] pre-trained on ImageNet as the backbone. For the multi-scale prototype learning, we assign $M = 3$ scale-dependent prototypes per scale to each class and $S = 4$ scales, so 12 prototypes per class in total. Moreover, we set the number of groups per class to $N_c = 3$ for the grouping mechanism. We evaluate ScaleProtoSeg on (i) Pascal VOC 2012 [21] (made of 1464 train, 1449 validation, and 1446 test images with 21 classes; the Pascal VOC training set is extended to 10582 images following [29]), (ii) Cityscapes [14] (composed of 2975 train, 500 validation, and 1525 test images of street scenes, with 19 classes) and (iii) ADE20K (a scene-parsing dataset with 150 fine-grained semantic classes split in ~ 20000 training and 2000 validation images; for the training of ProtoSeg [70] on ADE20K we extend the number of prototypes to 12 for direct comparison with ScaleProtoSeg). A detailed description of the experimental setup is available in the supplementary materials in Section 6.

4.2. Results and discussion

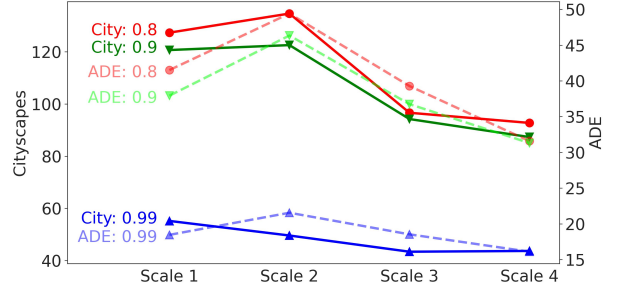
Method Performance. In Table 1, we present the performance of our interpretable semantic segmentation method ScaleProtoSeg. Due to the well-known lack of faithfulness of saliency-based methods [1, 68] and the difficulty to compare against other by-design methods not based on prototypes (different benchmark datasets, different backbones and/or lack of public code repositories) [56, 71], we compare ScaleProtoSeg against ProtoSeg [70] (the closest previous methods in the literature aimed at prototype-based interpretability for semantic segmentation) and the non-interpretable counterpart DeepLabv2 [9]. It is worth mentioning that, as interpretability comes at the price of constrained and regularized training (namely through prototype projection to real training samples, the use of the diversity loss, and the sparse grouping mechanism), an interpretable model aims to close the gap with the non-interpretable counterpart, which acts as an upper-bound. In this regard, ScaleProtoSeg showcases a substantial improvement over ProtoSeg in terms of mIoU for Cityscapes and ADE20K, namely of $\sim 1.5\%$ and 4% . For ADE20K, the proposed ScaleProtoSeg goes beyond its original goal of enabling interpretability by surpassing the performance of its black-box counterpart. The Cityscapes and ADE20K datasets present more natural images with numerous objects at various scales, unlike in Pascal, where our method provides less of an advantage (results are on par with those of ProtoSeg). Indeed, we hypothesize that learning explicitly scale-specific prototypes at multiple scales is more advantageous in segmentation tasks with a large depth of field. In the supplementary materials, we further demonstrate the transferability of ScaleProtoSeg (a) to the medical domain, (b) to another segmentation architecture and (c) to a larger benchmark dataset (COCO-Stuff) in Section 7 and 8.

This observation is confirmed by the results presented in Table 2, which showcases the high improvement brought by the projection step of ScaleProtoSeg, performed during the proposed multi-scale prototype learning (see Figure 2: **Stage 1**). This improvement comes with an increase of solely two prototypes per class from 190 to 228 prototypes on Pascal VOC and 210 (201 after deduplication) to 252 on Cityscapes. Furthermore, in Table 2 we observe that, through the grouping mechanism and thresholding, we reduce the total number of prototypes used by our model by 51.3%, 48.0%, and 37.1% for Cityscapes, Pascal, and ADE20K respectively, compared to 32.6%, 36.7%, and 35.5% for ProtoSeg after deduplication and pruning. As a result, ScaleProtoSeg uses fewer prototypes than ProtoSeg despite a higher initial count except for ADE20K (see Section 4.1). The proposed grouping mechanism (see Figure 2: **Stage 2**) trades better interpretability and simplified decision process (interaction of only 3 groups per class) with only 0.4% to 0.8% mIoU loss.

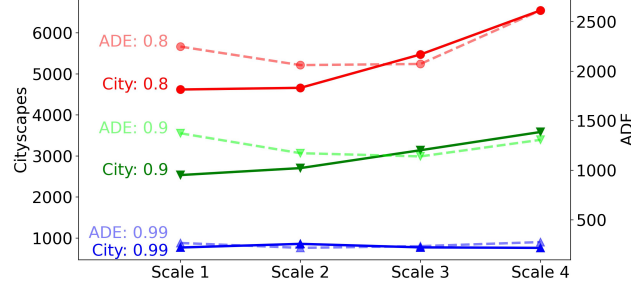
Method	Cityscapes		Pascal		ADE20K
	mIoU val	mIoU test	mIoU val	mIoU test	mIoU val
DeepLabv2 [9]	71.40	70.40	77.69	79.70	34.00
ProtoSeg [70]	67.54 ± 0.22	67.04	71.98 ± 0.11	72.92	29.67 ± 0.23
ScaleProtoSeg	68.97 ± 0.25	68.52	71.80 ± 0.38	72.35	34.18 ± 0.18

Table 1. ScaleProtoSeg mIoU performance on Pascal VOC, Cityscapes, and ADE20K. On the validation sets, we report the results over 3 runs, while for the test sets the results are based on [70] and our best ScaleProtoSeg validation run.

In the supplementary materials, we detail the capability of controlling the sparsity-performance trade-off via the thresholding of the grouping weights matrices and the entropy regularization in Section 9 and 10.



(a) Per-scale average number of connected components



(b) Per-scale average pixel area of the connected components

Figure 3. Analysis of the binarized prototype activations at multiple percentile thresholds $p_{th} \in \{0.8, 0.9, 0.99\}$ on Cityscapes and ADE20K validation sets.

Multi-Scale prototypes analysis. After the prototype projection at the end of the multi-scale prototype learning stage, different patterns of prototype activations emerge across scales. In Figure 3, we present a quantitative analysis of the prototype activations scale-specific patterns on Cityscapes and ADE20k. For this purpose, we first binarize the activation maps of the multi-scale prototype layer from ScaleProtoSeg on the validation set of both datasets: we do so with multiple percentiles $p_{th} \in \{0.8, 0.9, 0.99\}$. Then we measure the number of connected components in the binarized maps as well as their average area in number of pix-

Dataset	Cityscapes				Pascal				ADE20K			
Method	ProtoSeg		ScaleProtoSeg		ProtoSeg		ScaleProtoSeg		ProtoSeg		ScaleProtoSeg	
Step	project	pruned	project	grouped	project	pruned	project	grouped	project	pruned	project	grouped
Prototypes	190	128	228	111	201	133	252	131	1756	1161	1800	1132
mIoU	67.24	67.23	70.01	69.22	72.00	72.05	72.94	72.26	30.89	29.97	34.72	34.32

Table 2. Methods performance at different training steps based on the results from [70] and our best ScaleProtoSeg run. The number of prototypes indicated in the *project* step (during **Stage 1**) is after the duplicate removal. The number of prototypes in the *grouped* step (during **Stage 2**) corresponds to a threshold of 0.05 on the group matrices.

els. The average results per scale across all scale-specific prototypes are displayed in Figure 3.

We compute the connected components with the standard algorithm from *opencv* with an 8-connectivity relation between non-zero elements. We observe an overall decrease in the number of connected components when going from *Scale 1* to *Scale 4* across all thresholds and datasets and an increase in the average pixel area of the detected components (especially for ADE20K, which is less focused on images with large depth of field). In practice, this can be interpreted as a consequence of the lower field of view of the feature maps specific to *Scale 1* compared to those of *Scale 4* in the ASPP [9], where each scale-specific feature map vector represents a smaller receptive field on the image with less context. As such, the prototypes specific to *Scale 1* can be activated by smaller-scale prototypical parts and texture components. This analysis reflects the advantage of learning explicitly scale-specific prototypes across multiple scales: not only ScaleProtoSeg shows a performance improvement (see Table 2), but it also learns diverse object representations across scales, highlighting the multi-scale nature of semantic segmentation. In the supplementary material, we also analyzed if the prototypes present equivariance properties across scales in Section 11.

Quantitative analysis of interpretability. The quantitative evaluation of interpretability is an intrinsic problem in the field of XAI [1, 20] and especially in the context of per-design methods such as prototypical-parts learning [45, 91]. Several studies proposed human-based evaluations of explainable methods for classification tasks [13, 15]. However, scaling those evaluation scenarios to semantic segmentation raises concerns due to the complexity of the necessary human feedback compared to classification. We propose to quantitatively assess the degree of interpretability in terms of *consistency*, *stability*, and *sparsity*. The first two metrics have been proposed in [37] to measure the interpretability of a classification model. We leverage the part-annotations extension of Pascal and Cityscapes [16, 58] covering respectively 16 and 5 classes, and propose an extension of these metrics to the task of semantic segmentation. Given an input image \mathbf{x} and a prototype \mathbf{p}_m , the prototype activation $g_{\text{proto}}(\mathbf{z}, \mathbf{p}_m)$, $\forall \mathbf{z} \in f(\mathbf{x})$ is binarized using multiple percentile thresholds: $\{70^{\text{th}}, 80^{\text{th}}, 90^{\text{th}}\}$ instead of a fixed size bounding box, as multiple objects of the same class can be

present in \mathbf{x} . We then compute the average consistency and stability scores across the multiple thresholds on the part-annotated validation sets for 3 runs per method, similarly to [37]. We also introduce a global sparsity metric that measures the number of active prototypes per class after thresholding the last linear layer absolute values with $\tau_{th} = 0.005$, which is similar to the sparsity ratio used as a measure of interpretations’ compactness in [61]. The measured sparsity is linked to several properties of interpretability: transparency [24], understandability [13, 15], and simplicity [60]. Despite this metrics not being exhaustive, our assessment shows that ScaleProtoSeg displays overall enhanced interpretability over ProtoSeg (see Table 3 and 4).

Methods:	Pascal		
	Consistency \uparrow	Stability \uparrow	Sparsity \downarrow
ProtoSeg	35.05 ± 1.44	73.45 ± 0.45	157.67 ± 3.40
ScaleProtoSeg	38.78 ± 1.68	76.30 ± 0.26	23.34 ± 5.22

Table 3. Consistency, stability, and sparsity scores on Pascal part-annotated sets.

Methods:	Cityscapes		
	Consistency \uparrow	Stability \uparrow	Sparsity \downarrow
ProtoSeg	34.48 ± 1.74	27.00 ± 1.58	134 ± 2.45
ScaleProtoSeg	31.11 ± 1.66	32.54 ± 2.36	12.91 ± 1.26

Table 4. Consistency, stability, and sparsity scores on Cityscapes part-annotated sets.

Qualitative analysis of grouping mechanism interpretability. In terms of interpretability, the groups can be first represented through specific visualization for each sample, as shown in Figure 4, where the images on the graph display the prototype activations for an input sample. Those activations are grouped per scale and provide local explanations for the model. Moreover, the edges in those visualizations are static for all samples assigned to the class *car* in Cityscapes, and so provide global explanations on the model behavior. In Figure 4, we can easily observe, despite the large number of prototypes compared to the model mean of 3.39, that different patterns emerge for each group. The first group focuses mainly on a prototype in *Scale 4* activated on the bottom part of the cars and another similar at *Scale 2*. The second group focuses on a prototype at *Scale 1*, which activates the top of the cars with another one similar at *Scale 3*. Lastly, the third group focuses on mul-

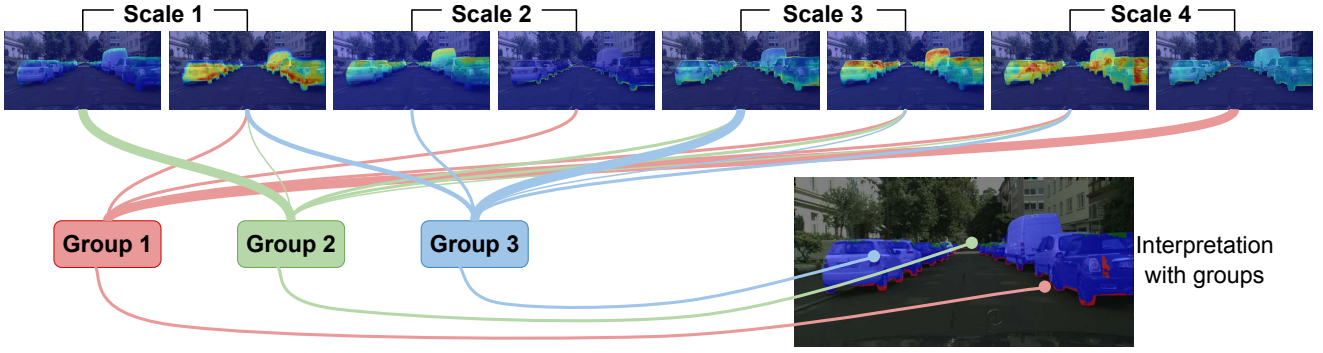


Figure 4. ScaleProtoSeg provides the interpretation of a segmentation through the analysis of groups of prototypes. For the example of the class *car* on Cityscapes, 2 prototypes per scale (whose activations are displayed **at the top** of the figure) are used by the model across the 3 learned groups shown **at the bottom right**. For this class, groups correspond to the bottom part, the main part or the upper part of the car.

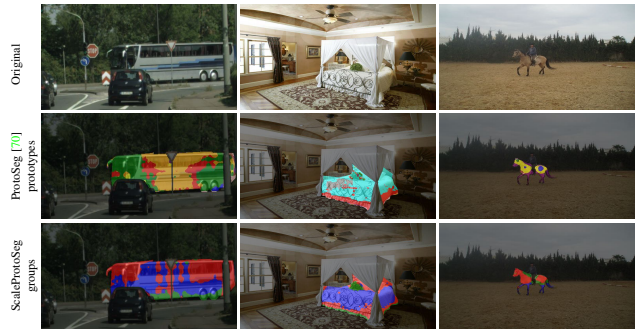


Figure 5. Model prototype and group assignments for the class *bus*, *bed*, and *horse* on Cityscapes, ADE20K, and Pascal.

multiple parts of the cars and, will activate on the main body of them. Groups 1 and 2, by combining similar prototypes across two scales, show transparently the use of multi-scale information in the model. Figure 4 demonstrates that the grouping mechanism in our method can be represented for both local and global interpretability. The example of group assignments for the class *car* illustrates the identified parts in the group visualization. Interestingly, the second group seems more activated on cars further in the depth field, as its main activated prototype is from *Scale 1* with a smaller field of view. This clearly illustrates the role of scale in the identification of prototypical parts.

In Figure 5, we show the final decision process based on the prototype assignments for ProtoSeg (row 2) and the group assignments for ScaleProtoSeg (row 3). The ProtoSeg outputs were computed based on a rerun of the model after pruning. In all three examples of Figure 5, our groups identify one or more prototypical parts each, for the class *bus*, *bed*, and *horse*. For instance, in the bus image, the first group in red corresponds to both the front and back top of the bus, a pattern that can be also seen in the other two images. Moreover, we see through those examples that, due

to the limited number of groups ($N_c = 3$) in ScaleProtoSeg, the interpretation of the final decision process is more constrained compared to the baseline method ProtoSeg. Indeed, even if we consider the prototype interactions leading to the group and their assignment, our method still uses fewer prototypes compared to ProtoSeg, as described in Table 2. Lastly, as detailed in the supplementary Section 12, our method enforces stronger sparsity regularization on the final classification layer inducing a smaller computation overhead on DeepLabv2 [9] compared to ProtoSeg [70].

Overall, through the sparsity of the groups, their simple visualizations, their small number, and the sparse final linear layer, we advocate that our method enables the user to investigate more transparently the semantic segmentation model while improving upon the state-of-the-art ProtoSeg.

5. Conclusion

In this paper, we present an interpretable semantic segmentation model, ScaleProtoSeg, that leverages multi-scale representations for prototype learning and introduces a novel grouping mechanism to learn prototype interactions across scales. We showed that our model results are particularly advantageous in complex datasets presenting many objects at different depths: Cityscapes and ADE20K. Moreover, through our analysis, we evaluated ScaleProtoSeg interpretability across 3 quantitative metrics: *consistency*, *stability*, and *sparsity* and inspected the different patterns learned by the prototypes across scales. This showcases the potential of multi-scale prototype learning to provide a deeper understanding of the effect of scales on object representations. Lastly, our novel grouping mechanism provides a clear representation of the final decision process: it shows how the model learns to group the prototypes across scales by limiting the number of active groups, allowing for their easy and sparse visualization for all images.

References

[1] Julius Adebayo, Justin Gilmer, Michael Muelly, Ian Goodfellow, Moritz Hardt, and Been Kim. Sanity checks for saliency maps. *Advances in neural information processing systems*, 31, 2018. 6, 7

[2] Julius Adebayo, Michael Muelly, Harold Abelson, and Been Kim. Post hoc explanations may be ineffective for detecting unknown spurious correlation. In *International conference on learning representations*, 2021. 1

[3] Rishabh Agarwal, Levi Melnick, Nicholas Frosst, Xuezhou Zhang, Ben Lengerich, Rich Caruana, and Geoffrey E Hinton. Neural additive models: Interpretable machine learning with neural nets. *Advances in neural information processing systems*, 34:4699–4711, 2021. 1, 2

[4] I Arganda-Carreras, HS Seung, A Cardona, and J Schindelin. Segmentation of neuronal structures in em stacks challenge-isbi 2012, 2012. 13, 14

[5] Miguel A Belenguer-Plomer, Mihai A Tanase, Angel Fernandez-Carrillo, and Emilio Chuvieco. Burned area detection and mapping using sentinel-1 backscatter coefficient and thermal anomalies. *Remote Sensing of Environment*, 233:111345, 2019. 1

[6] Andrea Bontempelli, Stefano Teso, Katya Tentori, Fausto Giunchiglia, and Andrea Passerini. Concept-level debugging of part-prototype networks. *arXiv preprint arXiv:2205.15769*, 2022. 18

[7] Holger Caesar, Jasper Uijlings, and Vittorio Ferrari. Coco-stuff: Thing and stuff classes in context. In *Proceedings of the IEEE conference on computer vision and pattern recognition*, pages 1209–1218, 2018. 14

[8] Chaofan Chen, Oscar Li, Daniel Tao, Alina Barnett, Cynthia Rudin, and Jonathan K Su. This looks like that: deep learning for interpretable image recognition. *Advances in neural information processing systems*, 32, 2019. 1, 2, 3, 4, 5

[9] Liang-Chieh Chen, George Papandreou, Iasonas Kokkinos, Kevin Murphy, and Alan L Yuille. Deeplab: Semantic image segmentation with deep convolutional nets, atrous convolution, and fully connected crfs. *IEEE transactions on pattern analysis and machine intelligence*, 40(4):834–848, 2017. 2, 3, 4, 5, 6, 7, 8, 13, 15

[10] Liang-Chieh Chen, Yukun Zhu, George Papandreou, Florian Schroff, and Hartwig Adam. Encoder-decoder with atrous separable convolution for semantic image segmentation. In *Proceedings of the European conference on computer vision (ECCV)*, pages 801–818, 2018. 2

[11] Bowen Cheng, Ishan Misra, Alexander G Schwing, Alexander Kirillov, and Rohit Girdhar. Masked-attention mask transformer for universal image segmentation. In *Proceedings of the IEEE/CVF conference on computer vision and pattern recognition*, pages 1290–1299, 2022. 1

[12] Bowen Cheng, Alex Schwing, and Alexander Kirillov. Per-pixel classification is not all you need for semantic segmentation. *Advances in Neural Information Processing Systems*, 34:17864–17875, 2021. 3

[13] Julien Colin, Thomas Fel, Rémi Cadène, and Thomas Serre. What i cannot predict, i do not understand: A human-centered evaluation framework for explainability methods. *Advances in neural information processing systems*, 35:2832–2845, 2022. 7

[14] Marius Cordts, Mohamed Omran, Sebastian Ramos, Timo Rehfeld, Markus Enzweiler, Rodrigo Benenson, Uwe Franke, Stefan Roth, and Bernt Schiele. The cityscapes dataset for semantic urban scene understanding. In *Proceedings of the IEEE conference on computer vision and pattern recognition*, pages 3213–3223, 2016. 2, 5, 13

[15] Omid Davoodi, Shayan Mohammadizadehsamakosh, and Majid Komeili. On the interpretability of part-prototype based classifiers: a human centric analysis. *Scientific Reports*, 13(1):23088, 2023. 7

[16] Daan de Geus, Panagiotis Meletis, Chenyang Lu, Xiaoxiao Wen, and Gijs Dubbelman. Part-aware panoptic segmentation. In *IEEE/CVF Conference on Computer Vision and Pattern Recognition (CVPR)*, 2021. 7, 13

[17] Henghui Ding, Xudong Jiang, Ai Qun Liu, Nadia Magnenat Thalmann, and Gang Wang. Boundary-aware feature propagation for scene segmentation. In *Proceedings of the IEEE/CVF International Conference on Computer Vision*, pages 6819–6829, 2019. 2

[18] Nanqing Dong and Eric P Xing. Few-shot semantic segmentation with prototype learning. In *BMVC*, volume 3, 2018. 3

[19] Jon Donnelly, Alina Jade Barnett, and Chaofan Chen. Deformable protopnet: An interpretable image classifier using deformable prototypes. In *Proceedings of the IEEE/CVF Conference on Computer Vision and Pattern Recognition*, pages 10265–10275, 2022. 2

[20] Finale Doshi-Velez and Been Kim. Towards a rigorous science of interpretable machine learning. *arXiv preprint arXiv:1702.08608*, 2017. 1, 7

[21] M. Everingham, L. Van Gool, C. K. I. Williams, J. Winn, and A. Zisserman. The PASCAL Visual Object Classes Challenge 2012 (VOC2012) Results. <http://www.pascal-network.org/challenges/VOC/voc2012/workshop/index.html>. 2, 5, 13

[22] Di Feng, Christian Haase-Schütz, Lars Rosenbaum, Heinz Hertlein, Claudius Glaeser, Fabian Timm, Werner Wiesbeck, and Klaus Dietmayer. Deep multi-modal object detection and semantic segmentation for autonomous driving: Datasets, methods, and challenges. *IEEE Transactions on Intelligent Transportation Systems*, 22(3):1341–1360, 2020. 1

[23] Jun Fu, Jing Liu, Haijie Tian, Yong Li, Yongjun Bao, Zhiwei Fang, and Hanqing Lu. Dual attention network for scene segmentation. In *Proceedings of the IEEE/CVF conference on computer vision and pattern recognition*, pages 3146–3154, 2019. 2

[24] Srishti Gautam, Ahcene Boubekki, Stine Hansen, Suaiba Salahuddin, Robert Janssen, Marina Höhne, and Michael Kampffmeyer. Protovae: A trustworthy self-explainable prototypical variational model. *Advances in Neural Information Processing Systems*, 35:17940–17952, 2022. 7

[25] Alan H Gee, Diego Garcia-Olano, Joydeep Ghosh, and David Paydarfar. Explaining deep classification of time-series data with learned prototypes. In *CEUR workshop*

proceedings, volume 2429, page 15. NIH Public Access, 2019. 2

[26] Marzyeh Ghassemi, Luke Oakden-Rayner, and Andrew L Beam. The false hope of current approaches to explainable artificial intelligence in health care. *The Lancet Digital Health*, 3(11):e745–e750, 2021. 1

[27] Yash Goyal, Ziyan Wu, Jan Ernst, Dhruv Batra, Devi Parikh, and Stefan Lee. Counterfactual visual explanations. In *International Conference on Machine Learning*, pages 2376–2384. PMLR, 2019. 1

[28] Ran Gu, Guotai Wang, Tao Song, Rui Huang, Michael Aertsen, Jan Deprest, Sébastien Ourselin, Tom Vercauteren, and Shaoting Zhang. Ca-net: Comprehensive attention convolutional neural networks for explainable medical image segmentation. *IEEE transactions on medical imaging*, 40(2):699–711, 2020. 2

[29] Bharath Hariharan, Pablo Arbeláez, Lubomir Bourdev, Subhransu Maji, and Jitendra Malik. Semantic contours from inverse detectors. In *2011 international conference on computer vision*, pages 991–998. IEEE, 2011. 5

[30] Peter Hase, Chaofan Chen, Oscar Li, and Cynthia Rudin. Interpretable image recognition with hierarchical prototypes. In *Proceedings of the AAAI Conference on Human Computation and Crowdsourcing*, volume 7, pages 32–40, 2019. 2

[31] Trevor Hastie and Robert Tibshirani. Generalized additive models: some applications. *Journal of the American Statistical Association*, 82(398):371–386, 1987. 2

[32] Junjun He, Zhongying Deng, Lei Zhou, Yali Wang, and Yu Qiao. Adaptive pyramid context network for semantic segmentation. In *Proceedings of the IEEE/CVF Conference on Computer Vision and Pattern Recognition*, pages 7519–7528, 2019. 2

[33] Kaiming He, Xiangyu Zhang, Shaoqing Ren, and Jian Sun. Deep residual learning for image recognition. In *Proceedings of the IEEE conference on computer vision and pattern recognition*, pages 770–778, 2016. 5

[34] Dan Hendrycks, Kevin Zhao, Steven Basart, Jacob Steinhardt, and Dawn Song. Natural adversarial examples. In *Proceedings of the IEEE/CVF Conference on Computer Vision and Pattern Recognition*, pages 15262–15271, 2021. 1

[35] Lukas Hoyer, Mauricio Munoz, Prateek Katiyar, Anna Khoreva, and Volker Fischer. Grid saliency for context explanations of semantic segmentation. *Advances in neural information processing systems*, 32, 2019. 1, 2

[36] Qin Huang, Chunyang Xia, Chihao Wu, Siyang Li, Ye Wang, Yuhang Song, and C-C Jay Kuo. Semantic segmentation with reverse attention. *arXiv preprint arXiv:1707.06426*, 2017. 13

[37] Qihan Huang, Mengqi Xue, Wenqi Huang, Haofei Zhang, Jie Song, Yongcheng Jing, and Mingli Song. Evaluation and improvement of interpretability for self-explainable part-prototype networks. In *Proceedings of the IEEE/CVF International Conference on Computer Vision*, pages 2011–2020, 2023. 7, 13

[38] Zilong Huang, Xinggang Wang, Lichao Huang, Chang Huang, Yunchao Wei, and Wenyu Liu. Ccnet: Criss-cross attention for semantic segmentation. In *Proceedings of the IEEE/CVF international conference on computer vision*, pages 603–612, 2019. 2

[39] Jyh-Jing Hwang, Stella X Yu, Jianbo Shi, Maxwell D Collins, Tien-Ju Yang, Xiao Zhang, and Liang-Chieh Chen. Segsort: Segmentation by discriminative sorting of segments. In *Proceedings of the IEEE/CVF International Conference on Computer Vision*, pages 7334–7344, 2019. 3

[40] Shipra Jain, Danda Pani Paudel, Martin Danelljan, and Luc Van Gool. Scaling semantic segmentation beyond 1k classes on a single gpu. In *Proceedings of the IEEE/CVF International Conference on Computer Vision*, pages 7426–7436, 2021. 3

[41] Harold Jeffreys. *The theory of probability*. OuP Oxford, 1998. 5

[42] Saumya Jetley, Bernardino Romera-Paredes, Sadeep Jayasumana, and Philip Torr. Prototypical priors: From improving classification to zero-shot learning. *arXiv preprint arXiv:1512.01192*, 2015. 3

[43] Jeya Vikranth Jeyakumar, Luke Dickens, Luis Garcia, Yu-Hsi Cheng, Diego Ramirez Echavarria, Joseph Noor, Alessandra Russo, Lance Kaplan, Erik Blasch, and Mani Srivastava. Automatic concept extraction for concept bottleneck-based video classification. *arXiv preprint arXiv:2206.10129*, 2022. 2

[44] Been Kim, Martin Wattenberg, Justin Gilmer, Carrie Cai, James Wexler, Fernanda Viegas, et al. Interpretability beyond feature attribution: Quantitative testing with concept activation vectors (tcav). In *International conference on machine learning*, pages 2668–2677. PMLR, 2018. 1

[45] Sunnie SY Kim, Nicole Meister, Vikram V Ramaswamy, Ruth Fong, and Olga Russakovsky. Hive: evaluating the human interpretability of visual explanations. *arXiv preprint arXiv:2112.03184*, 2021. 7

[46] Pang Wei Koh, Thao Nguyen, Yew Siang Tang, Stephen Mussmann, Emma Pierson, Been Kim, and Percy Liang. Concept bottleneck models. In *International conference on machine learning*, pages 5338–5348. PMLR, 2020. 1, 2

[47] Alexey Kurakin, Ian J Goodfellow, and Samy Bengio. Adversarial examples in the physical world. In *Artificial intelligence safety and security*, pages 99–112. Chapman and Hall/CRC, 2018. 1

[48] Nataliia Kussul, Mykola Lavreniuk, Sergii Skakun, and Andrii Shelestov. Deep learning classification of land cover and crop types using remote sensing data. *IEEE Geoscience and Remote Sensing Letters*, 14(5):778–782, 2017. 1

[49] Sebastian Lapuschkin, Stephan Wäldchen, Alexander Binder, Grégoire Montavon, Wojciech Samek, and Klaus-Robert Müller. Unmasking clever hans predictors and assessing what machines really learn. *Nature communications*, 10(1):1096, 2019. 1

[50] Junnan Li, Pan Zhou, Caiming Xiong, and Steven CH Hoi. Prototypical contrastive learning of unsupervised representations. *arXiv preprint arXiv:2005.04966*, 2020. 3

[51] Oscar Li, Hao Liu, Chaofan Chen, and Cynthia Rudin. Deep learning for case-based reasoning through prototypes: A neural network that explains its predictions. In *Proceed-*

ings of the AAAI Conference on Artificial Intelligence, volume 32, 2018. 2

[52] Guosheng Lin, Anton Milan, Chunhua Shen, and Ian Reid. Refinenet: Multi-path refinement networks for high-resolution semantic segmentation. In *Proceedings of the IEEE conference on computer vision and pattern recognition*, pages 1925–1934, 2017. 2

[53] Pantelis Linardatos, Vasilis Papastefanopoulos, and Sotiris Kotsiantis. Explainable ai: A review of machine learning interpretability methods. *Entropy*, 23(1):18, 2020. 1

[54] Sifei Liu, Shalini De Mello, Jinwei Gu, Guangyu Zhong, Ming-Hsuan Yang, and Jan Kautz. Learning affinity via spatial propagation networks. *Advances in Neural Information Processing Systems*, 30, 2017. 2

[55] Jonathan Long, Evan Shelhamer, and Trevor Darrell. Fully convolutional networks for semantic segmentation. In *Proceedings of the IEEE conference on computer vision and pattern recognition*, pages 3431–3440, 2015. 2

[56] Max Losch, Mario Fritz, and Bernt Schiele. Interpretability beyond classification output: Semantic bottleneck networks. *arXiv preprint arXiv:1907.10882*, 2019. 2, 6

[57] Diego Marcos, Ruth Fong, Sylvain Lobry, Rémi Flamary, Nicolas Courty, and Devis Tuia. Contextual semantic interpretability. In *Proceedings of the Asian Conference on Computer Vision*, 2020. 2, 4

[58] Panagiotis Meletis, Xiaoxiao Wen, Chenyang Lu, Daan de Geus, and Gijs Dubbelman. Cityscapes-panoptic-parts and pascal-panoptic-parts datasets for scene understanding. 7, 13

[59] Pascal Mettes, Elise Van der Pol, and Cees Snoek. Hyper-spherical prototype networks. *Advances in neural information processing systems*, 32, 2019. 3

[60] Yao Ming, Panpan Xu, Huamin Qu, and Liu Ren. Interpretable and steerable sequence learning via prototypes. In *Proceedings of the 25th ACM SIGKDD International Conference on Knowledge Discovery & Data Mining*, pages 903–913, 2019. 2, 7

[61] Meike Nauta, Jörg Schlötterer, Maurice Van Keulen, and Christin Seifert. Pip-net: Patch-based intuitive prototypes for interpretable image classification. In *Proceedings of the IEEE/CVF Conference on Computer Vision and Pattern Recognition*, pages 2744–2753, 2023. 7

[62] Tuomas Oikarinen, Subhro Das, Lam M Nguyen, and Tsui-Wei Weng. Label-free concept bottleneck models. *arXiv preprint arXiv:2304.06129*, 2023. 2

[63] Jeremy Petch, Shuang Di, and Walter Nelson. Opening the black box: the promise and limitations of explainable machine learning in cardiology. *Canadian Journal of Cardiology*, 38(2):204–213, 2022. 1

[64] René Ranftl, Alexey Bochkovskiy, and Vladlen Koltun. Vision transformers for dense prediction. In *Proceedings of the IEEE/CVF international conference on computer vision*, pages 12179–12188, 2021. 1, 2

[65] Dmitry Rashkovetsky, Florian Mauracher, Martin Langer, and Michael Schmitt. Wildfire detection from multisensor satellite imagery using deep semantic segmentation. *IEEE Journal of Selected Topics in Applied Earth Observations and Remote Sensing*, 14:7001–7016, 2021. 1

[66] Mattia Rigotti, Christoph Mikovic, Ioana Giurgiu, Thomas Gschwind, and Paolo Scotton. Attention-based interpretability with concept transformers. In *International Conference on Learning Representations*, 2021. 2

[67] Olaf Ronneberger, Philipp Fischer, and Thomas Brox. U-net: Convolutional networks for biomedical image segmentation. In *Medical Image Computing and Computer-Assisted Intervention–MICCAI 2015: 18th International Conference, Munich, Germany, October 5–9, 2015, Proceedings, Part III 18*, pages 234–241. Springer, 2015. 2, 13

[68] Cynthia Rudin. Stop explaining black box machine learning models for high stakes decisions and use interpretable models instead. *Nature machine intelligence*, 1(5):206–215, 2019. 1, 6

[69] Dawid Rymarczyk, Łukasz Struski, Jacek Tabor, and Bartosz Zieliński. Protopshare: Prototypical parts sharing for similarity discovery in interpretable image classification. In *Proceedings of the 27th ACM SIGKDD Conference on Knowledge Discovery & Data Mining*, pages 1420–1430, 2021. 2

[70] Mikołaj Sacha, Dawid Rymarczyk, Łukasz Struski, Jacek Tabor, and Bartosz Zieliński. Protoseg: Interpretable semantic segmentation with prototypical parts. In *Proceedings of the IEEE/CVF Winter Conference on Applications of Computer Vision*, pages 1481–1492, 2023. 1, 2, 3, 4, 5, 6, 7, 8, 13, 16, 19, 20

[71] Alberto Santamaría-Pang, James Kubricht, Aritra Chowdhury, Chitresh Bhushan, and Peter Tu. Towards emergent language symbolic semantic segmentation and model interpretability. In *Medical Image Computing and Computer Assisted Intervention–MICCAI 2020: 23rd International Conference, Lima, Peru, October 4–8, 2020, Proceedings, Part I 23*, pages 326–334. Springer, 2020. 1, 2, 6

[72] Ramprasaath R Selvaraju, Michael Cogswell, Abhishek Das, Ramakrishna Vedantam, Devi Parikh, and Dhruv Batra. Grad-cam: Visual explanations from deep networks via gradient-based localization. In *Proceedings of the IEEE international conference on computer vision*, pages 618–626, 2017. 1

[73] Sofia Serrano and Noah A Smith. Is attention interpretable? *arXiv preprint arXiv:1906.03731*, 2019. 2

[74] Mennatullah Siam, Mostafa Gamal, Moemen Abdel-Razek, Senthil Yogamani, Martin Jagersand, and Hong Zhang. A comparative study of real-time semantic segmentation for autonomous driving. In *Proceedings of the IEEE conference on computer vision and pattern recognition workshops*, pages 587–597, 2018. 1

[75] Jake Snell, Kevin Swersky, and Richard Zemel. Prototypical networks for few-shot learning. *Advances in neural information processing systems*, 30, 2017. 3

[76] Gregor Stiglic, Primoz Kocbek, Nino Fijacko, Marinka Zitnik, Katrien Verbert, and Leona Cilar. Interpretability of machine learning-based prediction models in healthcare. *Wiley Interdisciplinary Reviews: Data Mining and Knowledge Discovery*, 10(5):e1379, 2020. 1

[77] Robin Strudel, Ricardo Garcia, Ivan Laptev, and Cordelia Schmid. Segmenter: Transformer for semantic segmenta-

tion. In *Proceedings of the IEEE/CVF international conference on computer vision*, pages 7262–7272, 2021. 3

[78] Towaki Takikawa, David Acuna, Varun Jampani, and Sanja Fidler. Gated-scnn: Gated shape cnns for semantic segmentation. In *Proceedings of the IEEE/CVF international conference on computer vision*, pages 5229–5238, 2019. 2

[79] Pin Tang, Hai-Ming Xu, and Chao Ma. Prototransfer: Cross-modal prototype transfer for point cloud segmentation. In *Proceedings of the IEEE/CVF International Conference on Computer Vision*, pages 3337–3347, 2023. 3

[80] Yin Tang, Tao Chen, Xiruo Jiang, Yazhou Yao, Guo-Sen Xie, and Heng-Tao Shen. Holistic prototype attention network for few-shot vos. *arXiv preprint arXiv:2307.07933*, 2023. 3

[81] Michael Treml, José Arjona-Medina, Thomas Unterthiner, Rupesh Durgesh, Felix Friedmann, Peter Schubert, Andreas Mayr, Martin Heusel, Markus Hofmarcher, Michael Widrich, et al. Speeding up semantic segmentation for autonomous driving. 2016. 1

[82] Devis Tuia, Ribana Roscher, Jan Dirk Wegner, Nathan Jacobs, Xiaoxiang Zhu, and Gustau Camps-Valls. Toward a collective agenda on ai for earth science data analysis. *IEEE Geoscience and Remote Sensing Magazine*, 9(2):88–104, 2021. 1

[83] Kira Vinogradova, Alexandr Dibrov, and Gene Myers. Towards interpretable semantic segmentation via gradient-weighted class activation mapping (student abstract). In *Proceedings of the AAAI conference on artificial intelligence*, volume 34, pages 13943–13944, 2020. 1, 2

[84] Jiaqi Wang, Huafeng Liu, Xinyue Wang, and Liping Jing. Interpretable image recognition by constructing transparent embedding space. In *Proceedings of the IEEE/CVF International Conference on Computer Vision*, pages 895–904, 2021. 2

[85] Kaixin Wang, Jun Hao Liew, Yingtian Zou, Daquan Zhou, and Jiashi Feng. Panet: Few-shot image semantic segmentation with prototype alignment. In *proceedings of the IEEE/CVF international conference on computer vision*, pages 9197–9206, 2019. 3

[86] Wenhui Wang, Jifeng Dai, Zhe Chen, Zhenhang Huang, Zhiqi Li, Xizhou Zhu, Xiaowei Hu, Tong Lu, Lewei Lu, Hongsheng Li, et al. Internimage: Exploring large-scale vision foundation models with deformable convolutions. In *Proceedings of the IEEE/CVF Conference on Computer Vision and Pattern Recognition*, pages 14408–14419, 2023. 1

[87] Wenguan Wang, Cheng Han, Tianfei Zhou, and Dongfang Liu. Visual recognition with deep nearest centroids. *arXiv preprint arXiv:2209.07383*, 2022. 3

[88] Zhirong Wu, Yuanjun Xiong, Stella X Yu, and Dahua Lin. Unsupervised feature learning via non-parametric instance discrimination. In *Proceedings of the IEEE conference on computer vision and pattern recognition*, pages 3733–3742, 2018. 3

[89] Enze Xie, Wenhui Wang, Zhiding Yu, Anima Anandkumar, Jose M Alvarez, and Ping Luo. Segformer: Simple and efficient design for semantic segmentation with transform-
ers. *Advances in Neural Information Processing Systems*, 34:12077–12090, 2021. 1, 2

[90] Wenjia Xu, Yongqin Xian, Jiuniu Wang, Bernt Schiele, and Zeynep Akata. Attribute prototype network for zero-shot learning. *Advances in Neural Information Processing Systems*, 33:21969–21980, 2020. 3

[91] Romain Xu-Darme, Georges Quénot, Zakaria Chihani, and Marie-Christine Rousset. Sanity checks and improvements for patch visualisation in prototype-based image classification. *arXiv preprint arXiv:2302.08508*, 2023. 7

[92] Hong-Ming Yang, Xu-Yao Zhang, Fei Yin, and Cheng-Lin Liu. Robust classification with convolutional prototype learning. In *Proceedings of the IEEE conference on computer vision and pattern recognition*, pages 3474–3482, 2018. 3

[93] Changqian Yu, Jingbo Wang, Chao Peng, Changxin Gao, Gang Yu, and Nong Sang. Learning a discriminative feature network for semantic segmentation. In *Proceedings of the IEEE conference on computer vision and pattern recognition*, pages 1857–1866, 2018. 2

[94] Fisher Yu and Vladlen Koltun. Multi-scale context aggregation by dilated convolutions. *arXiv preprint arXiv:1511.07122*, 2015. 2

[95] Hang Zhang, Kristin Dana, Jianping Shi, Zhongyue Zhang, Xiaogang Wang, Ambrish Tyagi, and Amit Agrawal. Context encoding for semantic segmentation. In *Proceedings of the IEEE conference on Computer Vision and Pattern Recognition*, pages 7151–7160, 2018. 2

[96] Hengshuang Zhao, Jianping Shi, Xiaojuan Qi, Xiaogang Wang, and Jiaya Jia. Pyramid scene parsing network. In *Proceedings of the IEEE conference on computer vision and pattern recognition*, pages 2881–2890, 2017. 2

[97] Hengshuang Zhao, Yi Zhang, Shu Liu, Jianping Shi, Chen Change Loy, Dahua Lin, and Jiaya Jia. Psanet: Pointwise spatial attention network for scene parsing. In *Proceedings of the European conference on computer vision (ECCV)*, pages 267–283, 2018. 2

[98] Heliang Zheng, Jianlong Fu, Tao Mei, and Jiebo Luo. Learning multi-attention convolutional neural network for fine-grained image recognition. In *Proceedings of the IEEE international conference on computer vision*, pages 5209–5217, 2017. 2

[99] Bolei Zhou, Aditya Khosla, Agata Lapedriza, Aude Oliva, and Antonio Torralba. Learning deep features for discriminative localization. In *Proceedings of the IEEE conference on computer vision and pattern recognition*, pages 2921–2929, 2016. 2

[100] Bolei Zhou, Hang Zhao, Xavier Puig, Sanja Fidler, Adela Barriuso, and Antonio Torralba. Scene parsing through ade20k dataset. In *Proceedings of the IEEE conference on computer vision and pattern recognition*, pages 633–641, 2017. 2, 13

[101] Tianfei Zhou, Wenguan Wang, Ender Konukoglu, and Luc Van Gool. Rethinking semantic segmentation: A prototype view. In *Proceedings of the IEEE/CVF Conference on Computer Vision and Pattern Recognition*, pages 2582–2593, 2022. 3

Supplementary: Multi-Scale Grouped Prototypes for Interpretable Semantic Segmentation

6. Details on experimental set-up

In this section, we provide the details of the experimental set-up briefly described in Section 4.1 to support reproducing the results.

Firstly, across all training stages, the prototypes are the same size as the output feature maps of the non-concatenated ASPP in DeepLabv2 [9]: $D = 64$. For both multi-scale prototype training and the grouping mechanism we leverage augmentation techniques, such as random horizontal flipping, cropping, and scaling images by a factor between $[0, 1.5]$ for Cityscapes [14] and Pascal VOC [21], and $[0, 2]$ for ADE20K [100]. The batch size used in all the training stages is 10 and we select the Adam optimizer with a weight decay of $5e^{-4}$, $\beta_1 = 0.9$, and $\beta_2 = 0.999$ for our experiments. Moreover, as the batch size in our experiments is limited, we freeze the batch normalization parameters of the ResNet-101 backbone due to its impact on performance.

For the multi-scale prototype training stage, we set the weights of the loss terms to $\lambda_{L1} = 1e^{-4}$ and $\lambda_J = 0.25$ following ProtoSeg on both Cityscapes and Pascal VOC, and $\lambda_{L1} = 1e^{-5}$ for ADE20K due to the large number of classes. For the datasets: Cityscapes and Pascal VOC, we run first the warm-up step for 3000 batch iterations with a fixed learning rate of $2.5e^{-4}$. The joint training step is run for 30000 batch iterations with an initial learning rate of $2.5e^{-5}$ for ResNet-101 and $2.5e^{-4}$ for the prototype and ASPP layers. For this step, we leverage a learning rate scheduler following the polynomial learning rate policy with $power = 0.9$. Lastly, the fine-tuning step is done over 2000 batch iterations extended to 6000 for Pascal with a fixed learning rate of $1e^{-5}$. For ADE20K we leverage the same learning rate and learning rate scheduler as for the other two datasets but we double the number of batch iterations compared to Cityscapes on all steps: 6000 batches for warm-up, 60000 batches for joint training, and 4000 batches for fine-tuning.

The training of ProtoSeg on ADE20K follows the same experimental set-up as the multi-scale prototype training stage described above and as mentioned in Section 4.1: 12 prototypes per class were used to match ScaleProtoSeg.

During the training of the grouping mechanism, we set the weights of the loss terms to $\lambda_{L1} = 1e^{-3}$ for Cityscapes and Pascal VOC, and $\lambda_{L1} = 1e^{-4}$ for ADE20K. Moreover, we set $\lambda_{ent} = 0.05$ for Cityscapes and Pascal VOC, and $\lambda_{ent} = 0.25$ for ADE20K. We run the warm-up stage to train the group projections for 2000 batch iterations with a fixed learning rate of $2.5e^{-4}$ for all datasets. Then, we run the fine-tuning stage for 30000 batches with a learning rate of $2.5e^{-4}$ and the same optimizer and scheduling policy as in the prototype joint training phase for all datasets.

We evaluate ScaleProtoSeg on Pascal VOC for which we set the training image resolution to 321×321 and the testing one to 513×513 . Moreover, we use multi-scale inputs [9] with scales $\{0.5, 0.75, 1\}$ during training. We also evaluate ScaleProtoSeg on Cityscapes, for this dataset, we do not use MSC input training, we set the training resolution to 513×513 and the testing one to 1024×2048 . Lastly, we evaluate ScaleProtoSeg and ProtoSeg on ADE20K with no MSC input, a training resolution of 512×512 , and at test time we resize the smallest size of the image to the training resolution and keep the aspect ratio. Lastly, the performance of DeepLabv2 on ADE20K was extracted from [36].

The interpretability evaluation of our method is done on the parts annotated validation sets from Cityscapes and PASCAL-Context [16, 58]. In particular, to align to the classes and images covered during training for Pascal, we tested on the overlap images between PASCAL VOC and PASCAL-Context and so used the semantic annotations from PASCAL VOC and the part annotations from [16, 58] for the 16 classes covered. This represents 925 validation images for Pascal. Moreover, the stability and consistency metrics require part keypoints in their formulation, for this purpose we leverage the standard algorithm from opencv with an 8-connectivity relation between non-zero elements to compute the centroids of every connected component in the part annotations, similar to Section 4.2. The prototype activations are computed using the images in their native size for both datasets and interpolated to their corresponding part annotation size. We leverage multiple binarization thresholds on the prototype activations as mentioned in Section 4.2 to improve the robustness of those metrics in terms of variance across runs and to avoid a strong dependency on a fixed hyperparameter contrary to the window size used in [37].

7. Transferability of ScaleProtoSeg

To demonstrate the transferability of the proposed ScaleProtoSeg method beyond the domain of natural images, we run experiments on a medical dataset. In particular, we use the EM segmentation challenge dataset from ISBI 2012 [4], containing 30 images of size 512×512 with 2 classes that are randomly split 2 times in 20 training and 10 validation images, similar to the experiment in ProtoSeg [70]. The architecture used as the backbone for this experiment is the original U-Net [67]. The applicability of ScaleProtoSeg to another segmentation backbone is straightforward as it simply requires stacking the ASPP at the network output before the classification layer, allowing the extraction of multi-scale feature maps. The prototype layer contains 10 and 12 prototypes per class for Proto-

toSeg and ScaleProtoSeg respectively, so 3 prototypes per scale and class for ScaleProtoSeg and similarly 3 groups per class. We run 3 experiments per method in the same set-up as in ProtoSeg with pruning and grouping for each method respectively. For the prototype training stage, we skip the warm-up step and run the joint training and fine-tuning step for 10000 batches iterations each with a batch size of 2. The learning rate for the joint step is fixed at $1e^{-4}$ and we use the same learning scheduler as in Section 6. The learning rate for the fine-tuning step is constant and fixed at $1e^{-5}$. The weights of the loss terms for both methods during the prototype training stage are set to $\lambda_{L1} = 1e^{-4}$ and $\lambda_J = 0.25$. In the grouping stage for ScaleProtoSeg, we also skip the warm-up step and run the joint training step for 10000 batch iterations with a learning of $5e^{-5}$ following the same scheduler as in Section 6. The weights of the loss terms during the grouping stage are set to $\lambda_{L1} = 1e^{-4}$ and $\lambda_{ent} = 0.25$. The optimizer and augmentation pipeline used across all stages and methods is the same as in Section 6. We report the mIoU in Table 5. Results show that *ScaleProtoSeg can transfer to another backbone and image modality*. Indeed, not only ScaleProtoSeg outperforms ProtoSeg in datasets with complex scenarios (CityScapes and ADE20K), but it also yields marginally better performance in the considered medical dataset despite the fact that the images do not present multi-scale features (similarly to the PASCAL VOC benchmark).

Method	EM Split 1	EM Split 2
ProtoSeg (U-Net + ASPP)	77.63 ± 0.29	78.92 ± 0.19
ScaleProtoSeg (U-Net + ASPP)	77.97 ± 0.16	79.29 ± 0.17

Table 5. IoU performance of ScaleProtoSeg compared against ProtoSeg. Results demonstrate the effective transferability of ScaleProtoSeg to another segmentation architecture (U-Net) and the medical domain (ISBI 2012 dataset) [4].

8. Extension to large dataset

In order to test our method in a use case close to real-world applications we extend our evaluation to a large benchmark: COCO-Stuff [7], containing 182 classes with 118k training and 5k validation samples. We leverage a similar setup to ADE20K for the model hyperparameters, except that in the multi-scale prototype training stage, we iterate for a total of 110k iterations: 6k warm-up steps, 100k joint steps, and 4k finetuning steps. Moreover, the iterations are done directly on a batch of size 10. We also use multi-scale inputs with scales $\{0.5, 0.75, 1\}$ and a training resolution of 321×321 , while testing at the native resolution. The objective is to align to the set-up for the DeepLabv2 baseline provided at this repository: github.com/kazuto1011/deeplab-pytorch. The results for our method: ScaleProtoSeg are presented in Table 6, and

Method	COCO-Stuff mIoU
DeepLabv2	39.7
ScaleProtoSeg	34.50 ± 0.19

Table 6. ScaleProtoSeg mIoU performance on COCO-Stuff validation set. We report the results over 3 runs for our method.

showcase that our method despite lower performance stays competitive with DeepLabv2 on a larger dataset while providing interpretability. Moreover, ProtoSeg trained in a similar set-up has a performance of 32.97 mIoU without pruning for one run, and so ScaleProtoSeg slightly outperforms it.

9. Sparsity Regularization

In the grouping mechanism, it is also possible to control for the sparsity-performance trade-off via the thresholding of the grouping weights in the matrices $\mathbf{w}_{g,c}$ defined in Section 3.2. This is demonstrated in Table 7. The best results are obtained for threshold $\alpha = 0.05$ on all datasets. At this threshold, the groups are sparse with an average of 3.70, 3.39, and 4.08 active prototypes per group for Pascal, Cityscapes, and ADE20K, which leads to better interpretability performance for the sparsity metric compared to ProtoSeg. Moreover, we analyze the effect of the entropy regularization on the grouping mechanism as shown in Table 8. This regularization enables our method to use fewer prototypes in total and per group while providing similar performance, with up to 20 total prototypes dropped and 2.5 prototypes per group less for Cityscapes.

Dataset	Threshold	Prototypes	Group Avg	mIoU
Pascal	$\alpha = 0.$	133	4.00	72.11
	$\alpha = 0.05$	131	3.70	72.26
	$\alpha = 0.1$	126	3.21	72.12
Cityscapes	$\alpha = 0.$	114	3.68	69.20
	$\alpha = 0.05$	111	3.39	69.22
	$\alpha = 0.1$	109	3.10	69.03
ADE20K	$\alpha = 0.$	1168	4.53	34.03
	$\alpha = 0.05$	1132	4.08	34.32
	$\alpha = 0.1$	1067	3.48	34.16

Table 7. Ablation study of the effect of thresholding on the grouping mechanism with $\lambda_{ent} = 0.05$ on our ScaleProtoSeg best performing run.

10. Group Overlap

In this section, we extend the analysis on the effect of the entropy loss regularization on the grouping mechanism presented above, as entropy regularization also impacts the overlap between group activations and supports identifying prototypical parts.

Dataset	Regularization	Prototypes	Group Avg	mIoU
Pascal	$\lambda_{\text{ent}} = 0$	146	5.59	72.22
	$\lambda_{\text{ent}} = 0.05$	131	3.70	72.26
Cityscapes	$\lambda_{\text{ent}} = 0$	132	5.79	69.22
	$\lambda_{\text{ent}} = 0.05$	111	3.39	69.22
ADE20K	$\lambda_{\text{ent}} = 0$	1405	6.06	33.40
	$\lambda_{\text{ent}} = 0.25$	1132	4.08	34.32

Table 8. Ablation study on the effect of the entropy regularization on the grouping mechanism with $\alpha = 0.05$ on our ScaleProtoSeg best performing run.

Dataset	Regularization	mIoU Groups
Pascal	$\lambda_{\text{ent}} = 0$	47.45
	$\lambda_{\text{ent}} = 0.05$	28.29
Cityscapes	$\lambda_{\text{ent}} = 0$	61.65
	$\lambda_{\text{ent}} = 0.05$	43.48
ADE20K	$\lambda_{\text{ent}} = 0$	50.25
	$\lambda_{\text{ent}} = 0.25$	42.74

Table 9. Analysis of the effect of the entropy regularization on the group activations overlap measured via mIoU with a threshold $\alpha = 0.05$ on our ScaleProtoSeg best performing run.

We observe that besides reducing the number of prototypes used in the groups as shown in Table 8, the entropy loss also encourages diversity in the activations of the groups assigned to the same class as shown in Figure 6 for Cityscapes. In Table 9, we present a quantitative analysis of this phenomenon. Firstly, on the validation sets of Pascal, Cityscapes, and ADE20K, we binarize all the group activations using the 95th percentile. Then we compute on those validation sets the mIoU between the binarized group activation maps assigned to the same class, as a measure of overlap in the group activations. We observe that the entropy regularization on all three datasets decreases the overlap between groups of up to 19% for Pascal. A low overlap between group activations enables the model to focus on different prototypical parts of the object and avoid groups all focusing on the whole object. Those results can be explained by the increased sparsity of the grouping functions, which ultimately leads to more variation in prototype assignment between the groups.

11. Multi-scale prototype analysis

In the proposed ScaleProtoSeg method, each set of prototypes assigned to a scale $s \in S$ corresponds to a specific field of view (FOV) from the ASPP layer in [9]. We hypothesize that certain class-specific prototypes form pairs or groups of quasi-equivariant prototype activations between scales. Our definition of quasi-equivariance across scales is as follows. For a class $c \in \mathcal{C}$, let us consider $\forall \mathbf{x} \in \mathbb{R}^{H \times W \times 3}$ and its downsampled version $\mathbf{x}' \in \mathbb{R}^{\frac{H}{2} \times \frac{W}{2} \times 3}$ (the factor of 2 here matched the atrous rate increase from scale

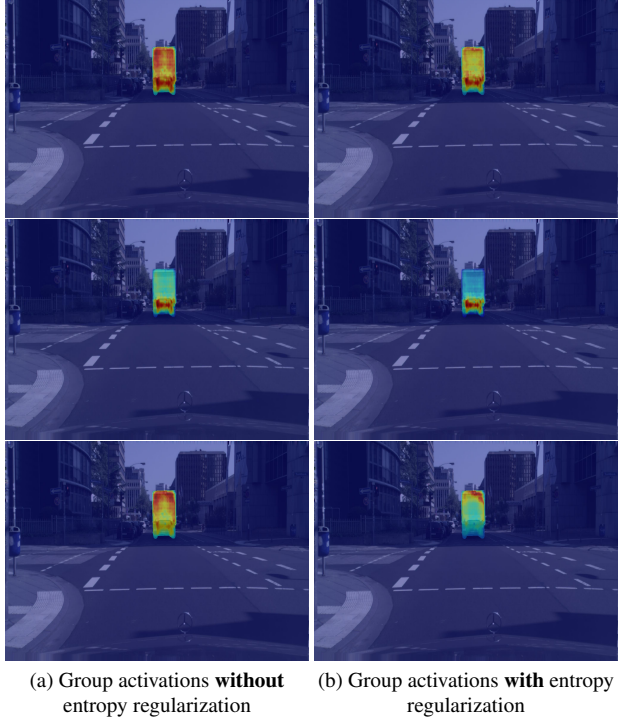


Figure 6. Example of group activations with or without entropy regularization for the class *truck* on Cityscapes.

1 to 2). Let us select the candidate pair of quasi-equivariant prototypes $\mathbf{p}_{1,i} \in P_{1,c}$ and $\mathbf{p}_{2,j} \in P_{2,c}$ and compute their respective activation maps $\mathbf{A}_{1,i}$ from all $\mathbf{z}_1 \in f_1(\mathbf{x}')$ with $g_{\text{proto}}(\mathbf{z}_1, \mathbf{p}_{1,i})$, and $\mathbf{A}_{2,j}$ from all $\mathbf{z}_2 \in f_2(\mathbf{x})$ with $g_{\text{proto}}(\mathbf{z}_2, \mathbf{p}_{2,j})$. The pair of prototypes is considered as quasi-equivariant if:

$$f_{\text{upsample}}(\mathbf{A}_{1,i}) \sim \mathbf{A}_{2,j} \quad (10)$$

with f_{upsample} the upsampling function for $\mathbf{A}_{1,i}$ to the original size of $\mathbf{A}_{2,j}$. The similarity measure between activations is defined below.

In order to identify the sets of prototypes with quasi-equivariant activations for a specific class $c \in \mathcal{C}$ we first specify the increasing atrous rates ratio of each ASPP output feature maps with respect to the smallest one: $\{r_{1 \rightarrow 1}, r_{1 \rightarrow 2}, r_{1 \rightarrow 3}, r_{1 \rightarrow 4}\}$ in the case of $S = 4$. The objective is to compute for all training images $\mathbf{x} \in \mathbb{R}^{H \times W \times 3}$, downsampled versions of the original image $\mathbf{x}_{1 \rightarrow s}$ such that $\mathbf{x}_{1 \rightarrow s} \in \mathbb{R}^{\frac{H}{r_{1 \rightarrow s}} \times \frac{W}{r_{1 \rightarrow s}} \times 3}$. Then, for all distinct pairs of feature map scales such that $(s, s') \in S^2$ and $s < s'$, we select $\mathbf{x}_{1 \rightarrow s}$ and $\mathbf{x}_{1 \rightarrow s'}$ to compute $f_s(\mathbf{x}_{1 \rightarrow s'})$ and $f_{s'}(\mathbf{x}_{1 \rightarrow s})$. The objective is to align, through the downscaling of the image, the semantic parts covered by the FOV of each ASPP scale s and s' . Then we compare all pairs of prototypes from the scales s and s' . For a specific pair $(\mathbf{p}_{s,i}, \mathbf{p}_{s',j})$ we compute from the feature maps $f_s(\mathbf{x}_{1 \rightarrow s'})$ and $f_{s'}(\mathbf{x}_{1 \rightarrow s})$, the acti-

vation maps $f_{\text{upsample}}(\mathbf{A}_{s,i})$ and $\mathbf{A}_{s',j}$, as described above. The similarity measure is then computed as follows, as we want to focus on the most activated parts for the objects assigned to c we threshold the activation maps to a percentile $p_{th} \in \{0.6, 0.7\}$ only considering the positions where the ground truth label $y_{\mathbf{z}} = c$. Then we derive the mIoU between the binarized activation maps across all the training set images, defining our similarity measure. Pairs of quasi-equivariant prototypes are identified when the mIoU is above a fixed threshold $\text{IoU}_{th} = 0.5$ on the training set. Lastly, pairs of quasi-equivariant prototypes are merged into groups if they overlap across scales.

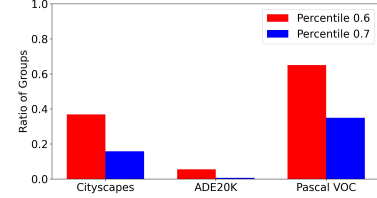
In Figure 7, we present the results of the equivariance analysis on three datasets. Interestingly, we observe that for both Cityscapes and Pascal VOC there are more than 50% of classes with quasi-equivariant groups for $p_{th} = 0.6$, demonstrating that the network learns through its multi-scale prototypes similar activations for similar prototypical parts in the image at different scales. For ADE20K, we observe that only 12% of classes have quasi-equivariant groups. We argue that since ADE20K is characterized by many complex scenes, as we constrain the representation space to the learning of only 12 prototypes across scales, all the learned prototypes represent scale-specific contextual information. We suppose that if we were to increase the number of prototypes per scale, redundant information would start to appear across scales and more prototypes would be activated on similar prototypical parts at different scales, leading to an increase in the number of classes with quasi-equivariant groups. In Figure 8, 9, and 10 we show examples of pair of quasi-equivariant prototypes for $p_{th} = 0.6$.

12. Sparsity and Computation Overhead

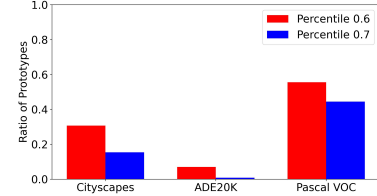
Dataset	Method	Avg Weight	Parameters	It/s
Pascal	ProtoSeg	0.527 ± 0.004	$12.1\text{K} \pm 0.3$	20.7 ± 0.2
	ScaleProtoSeg	0.063 ± 0.001	$9.1\text{K} \pm 0.0$	15.6 ± 0.5
Cityscapes	ProtoSeg	0.523 ± 0.001	$9.9\text{K} \pm 0.2$	52.5 ± 0.2
	ScaleProtoSeg	0.071 ± 0.001	$7.6\text{K} \pm 0.1$	5.1 ± 0.0
ADE20K	ProtoSeg	0.503 ± 0.001	$238.2\text{K} \pm 2.2$	51.9 ± 2.0
	ScaleProtoSeg	0.437 ± 0.001	$135.4\text{K} \pm 0.3$	14.5 ± 0.8

Table 10. Analysis of the sparsity of the final classification layer via the average absolute weight in $\mathbf{w}_{h_{\text{proto}}}$ for ProtoSeg and $\mathbf{w}_{h_{\text{group}}}$ for ScaleProtoSeg, and the computation overhead with respect to DeepLabv2 induced by the interpretable methods.

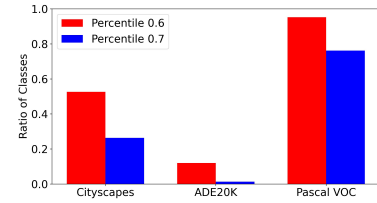
In the sparse grouping mechanism proposed in our method, we also enforce a strong sparsity regularization on the last layer h_{proto} which enables the model to constrain the negative effect of the prototypes not assigned to a class in the final decision process, as shown in Section 3.3. We see in Table 10 that our method presents a small average absolute weight on $\mathbf{w}_{h_{\text{group}}}$ and as a consequence a strong sparsity



(a) Ratio of quasi-equivariant groups identified.



(b) Ratio of prototypes in the quasi-equivariant groups.



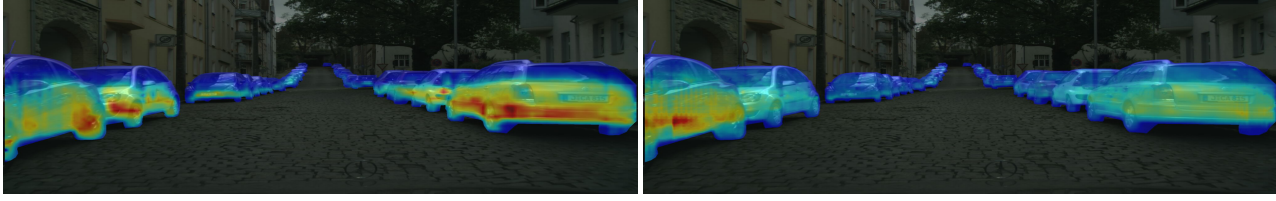
(c) Ratio of classes with quasi-equivariant groups.

Figure 7. Analysis of the presence of quasi-equivariant groups in all three datasets for $p_{th} \in \{0.6, 0.7\}$ on our best performing ScaleProtoSeg run. In (a), the number of quasi-equivariant groups is compared to the total number of groups defined in the sparse grouping mechanism.

for both Pascal VOC and Cityscapes, especially compared to ProtoSeg. Moreover, despite the increased complexity of ADE20K, our method presents still a smaller average absolute weight than ProtoSeg.

We also analyze in Table 10 the number of extra-parameters necessary in our method and ProtoSeg compared to the black-box baseline: DeepLabv2, after pruning at inference. We observe that, due to the limited number of active prototypes and the group projection, ScaleProtoSeg requires less computational overhead, especially for a large number of classes like in ADE20K, where our method uses 43% less extra parameters. Those results are computed on 3 local runs per method, and it is important to highlight that ProtoSeg on Pascal despite similar performance presents ~ 25 more prototypes after pruning compared to [70], which also directly impacts the sparsity metric in Table 6.

It is also important to consider the computational overhead during training. First, we showed that the added



(a) Prototype activations on a pair of quasi-equivariant prototypes for an input image downsampled by a ratio of 2 and 1 respectively.



(b) Binarized prototype activations on a pair of quasi-equivariant prototypes for an input image downsampled by a ratio of 2 and 1 respectively.

Figure 8. Example of quasi-equivariant pair of prototypes for the class *car* on Cityscapes. Prototype on the left is from *Scale 1* and on the right is from *Scale 2*.

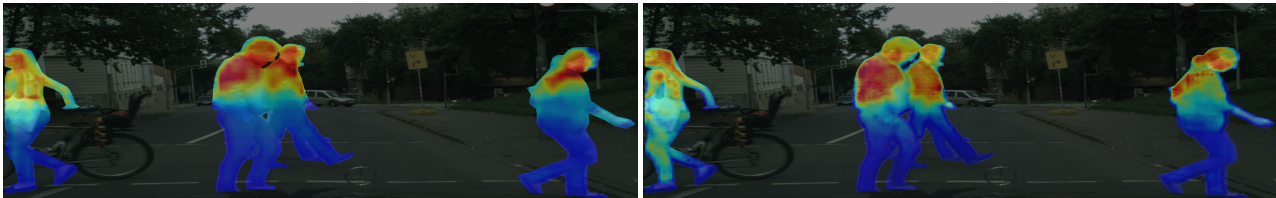


(a) Prototype activations on a pair of quasi-equivariant prototypes for an input image downsampled by a ratio of 3 and 1 respectively.



(b) Binarized prototype activations on a pair of quasi-equivariant prototypes for an input image downsampled by a ratio of 3 and 1 respectively.

Figure 9. Example of quasi-equivariant pair of prototypes for the class *rider* on Cityscapes. Prototype on the left is from *Scale 1* and on the right is from *Scale 3*.



(a) Prototype activations on a pair of quasi-equivariant prototypes for an input image downsampled by a ratio of 3 and 1 respectively.



(b) Binarized prototype activations on a pair of quasi-equivariant prototypes for an input image downsampled by a ratio of 3 and 1 respectively.

Figure 10. Example of quasi-equivariant pair of prototypes for the class *person* on Cityscapes. Prototype on the left is from *Scale 1* and on the right is from *Scale 3*.

number of parameters compared to DeepLabv2 is minimal. However, some overhead complexity arises in ProtoSeg and ScaleProto from the KLD regularisation loss and the prototype projection. In particular, the impact on training time of the KLD loss is much more important in the case of ProtoSeg at a high number of prototypes compared to ScaleProtoSeg as in our method we parallelize the loss across scales. Moreover, at training time the fine-tuning of the classification layer and groups after the prototype projection of our method adds only a limited overhead to the training as we tune only a handful of parameters for a few epochs.

Finally as shown in Table 10 at inference our method is slower than ProtoSeg due to the grouping process but we believe that is likely due to a lack of parallelization in our code.

13. Group Representations and Assignments

In this section, we aim to present more representative examples of our results in terms of interpretability. First, we show in Figure 11 an example of group activations for the class *person* in Cityscapes, where groups 1 and 2 identify the head and feet respectively of a *person*, while group 3 identifies the main body of the *persons*. Interestingly, similarly to the class *car* in the main paper, group 2 is mainly activated by a prototype at scale 1 and as a consequence seems to be more present on *person* further away in the image as seen in (b). This level of understanding of the scale effect on the model representation is a key contribution of our method compared to ProtoSeg in terms of interpretability.

Moreover, we show in Figure 12 and 13 more comparative results between our method and ProtoSeg, where again the limitations on the number of groups simplify the analysis of the decision process for our method as seen for the class *bicycle* and *chair*. In the analysis of the class *rider* and *aeroplane*, we can observe another advantage of our method as ProtoSeg presents a failure case of prototype pruning where only one prototype specific to the class *rider* or *aeroplane* is left after post-processing.

14. Nearest Image Patches to Prototypes

For the learned prototypes to be interpretable to the users, the semantic parts that they represent should be similar across images. To analyze whether our method is consistent across images, we extend the consistency metric from Section 4.2 with visualizations of the nearest images in the validation set from a few prototypes in Cityscapes and Pascal VOC. Those visualizations are shown in Figures [14 - 19], and showcase strong semantic correspondences between the prototypes and their closest patches.

15. Nearest Prototypes to Image Patches

To further analyze the semantic correspondences in the prototype layer of the model, we study the nearest prototypes to all image patches during the decision process. This is also directly linked to the consistency metric. To this purpose, in Figure [20 - 25] we visualize the three closest prototypes for random patches in an image. The visualizations again showcase good semantic matches for our proposed method.

16. Semantic meaning of groups

We provide a clearer understanding of the grouping mechanism by showing, in Figure 26, the activations of prototypes assigned to the same group for a given class. It can be observed that prototypes are grouped into semantically meaningful groups.

17. Failure case analysis

In this section, we analyze an image from PASCAL VOC where the IoU for a given class: cow, falls below a threshold set to $\epsilon_{IoU} = 0.2$, to describe how our method can be leveraged for interpretability analysis. For this failure, we observe in Figure 27 that the veal in the image is classified as a sheep. Indeed, we observe in Figure 28 that for the group activations of the class cow, only the first group is slightly activated essentially on the second cow behind, while the 3 sheep groups activate both the top and bottom of the animal. We observe that all the main prototypes for the cow groups in Figure [30 - 32] either activate a part not visible on the veal or seem to rather focus on the "texture" of the animal which can be misleading in this case. For the class sheep, we observed in Figure [33 - 35] that the two most activated groups: 1 and 3, are driven by the same prototype which is a Scale 1 prototype focusing on texture. This seems reasonable knowing that the wool is a characteristic specific to this class and that a similar aspect can be seen for the veal. To avoid learning misleading "texture" prototypes such as the one mentioned previously, the method presented in [6] can be leveraged to enforce forgetting such prototypes via human expert feedback.

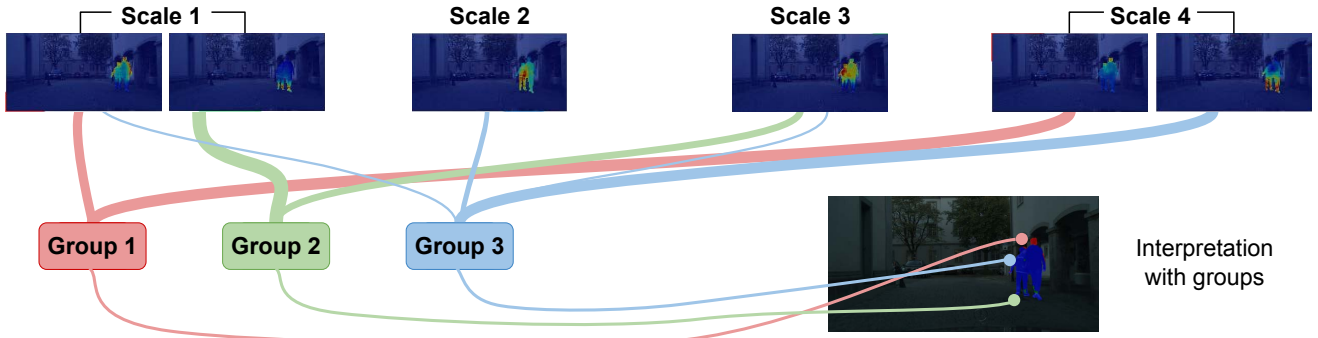


Figure 11. ScaleProtoSeg provides an interpretation of the resulted segmentation through groups of prototypes. For an example of the class *person* on Cityscapes, 2 prototypes per scale (whose activations are displayed **at the top** of the figure) are used by the model across the 3 learned groups shown **at the bottom right**. For this class, groups can correspond to the feet, the main body or the head of the person.



Figure 12. Model prototype, group assignments and prediction for the class *bicycle*, *rider*, and *chair* on Cityscapes, and ADE20K.



Figure 13. Model prototype, group assignments and prediction for the class *dinning table*, *aeroplane*, and *animal* on Pascal, and ADE20K.

Prototypes



Top 1 Patch



Top 2 Patch



Top 3 Patch



Figure 14. The first row represents a prototype for the class *person* in Cityscapes marked by a red box and the activation of the prototype on its image. The second to fourth rows show the closest patches to the prototype and its activation on the images containing the patches.

Prototypes



Top 1 Patch



Top 2 Patch



Top 3 Patch



Figure 15. The first row represents a prototype for the class *car* in Cityscapes marked by a red box and the activation of the prototype on its image. The second to fourth rows show the closest patches to the prototype and its activation on the images containing the patches.

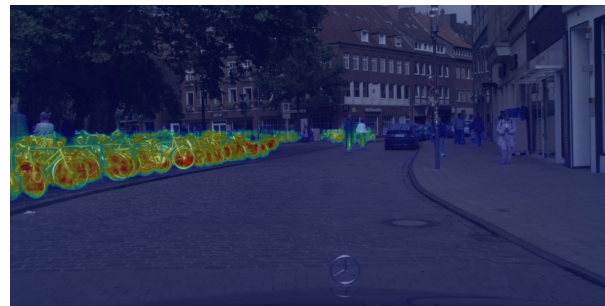
Prototypes



Top 1 Patch



Top 2 Patch



Top 3 Patch



Figure 16. The first row represents a prototype for the class *bicycle* in Cityscapes marked by a red box and the activation of the prototype on its image. The second to fourth rows show the closest patches to the prototype and its activation on the images containing the patches.

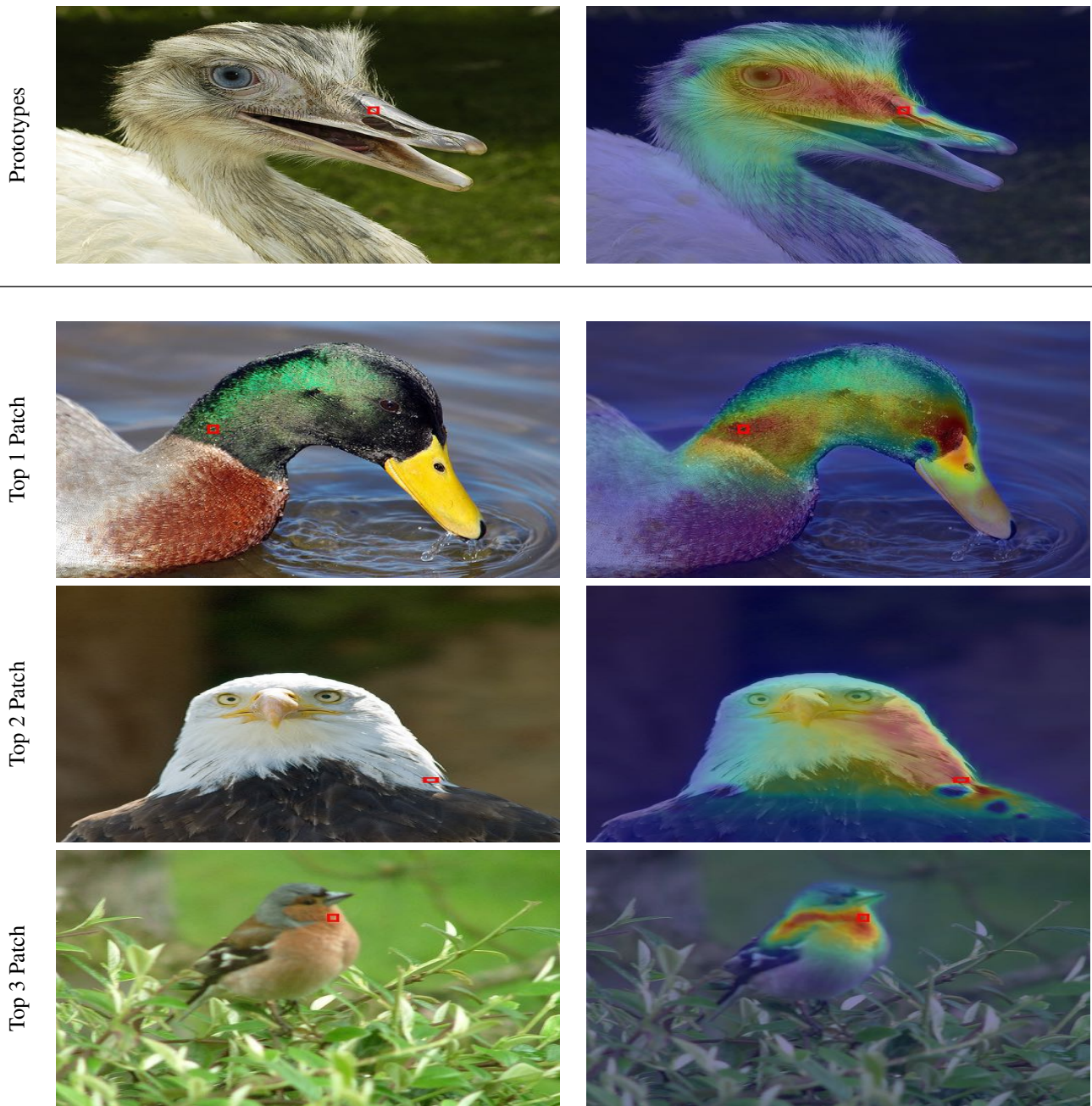


Figure 17. The first row represents a prototype for the class *bird* in PASCAL VOC marked by a red box and the activation of the prototype on its image. The second to fourth rows show the closest patches to the prototype and its activation on the images containing the patches.

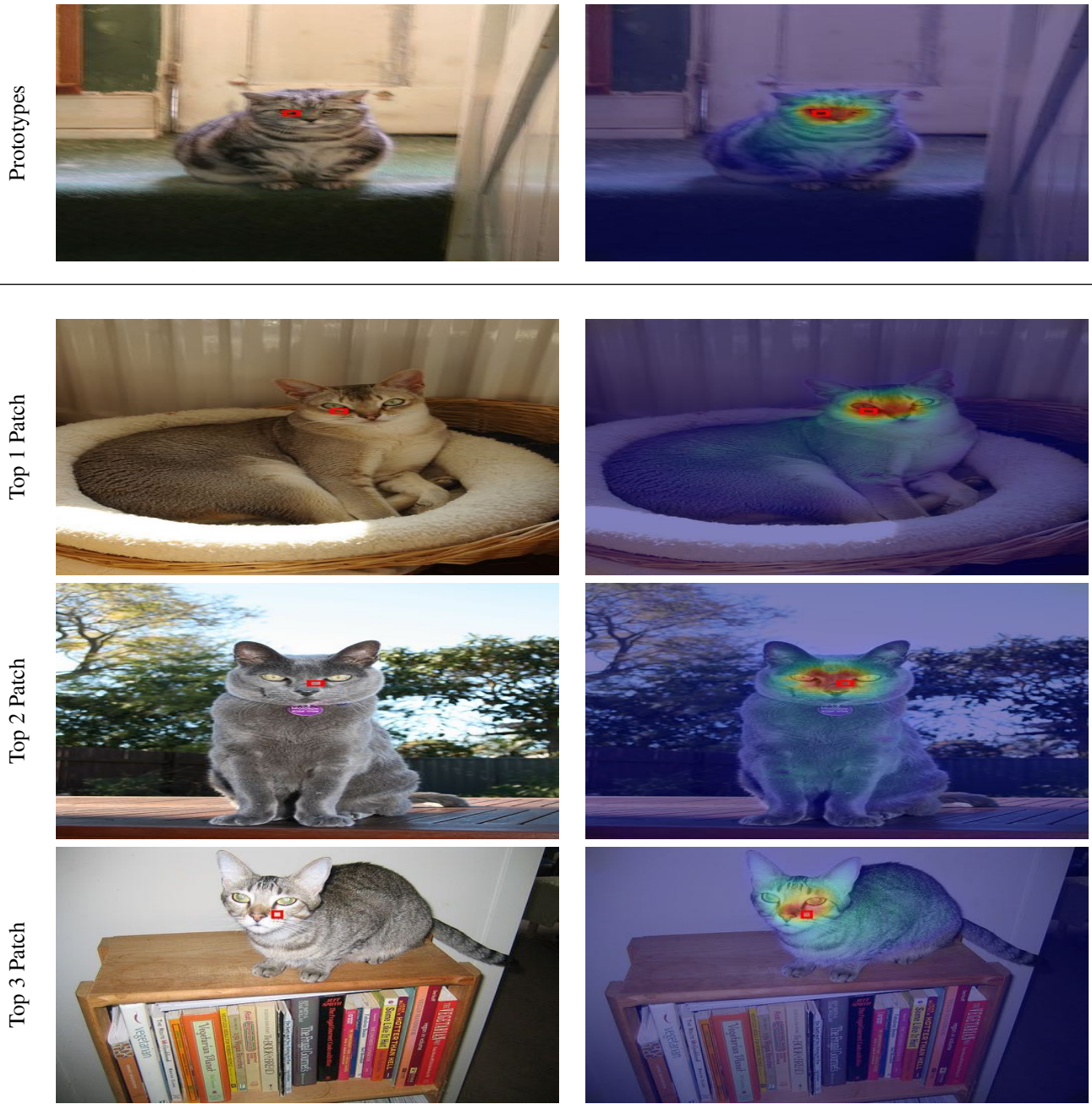


Figure 18. The first row represents a prototype for the class *cat* in PASCAL VOC marked by a red box and the activation of the prototype on its image. The second to fourth rows show the closest patches to the prototype and its activation on the images containing the patches.

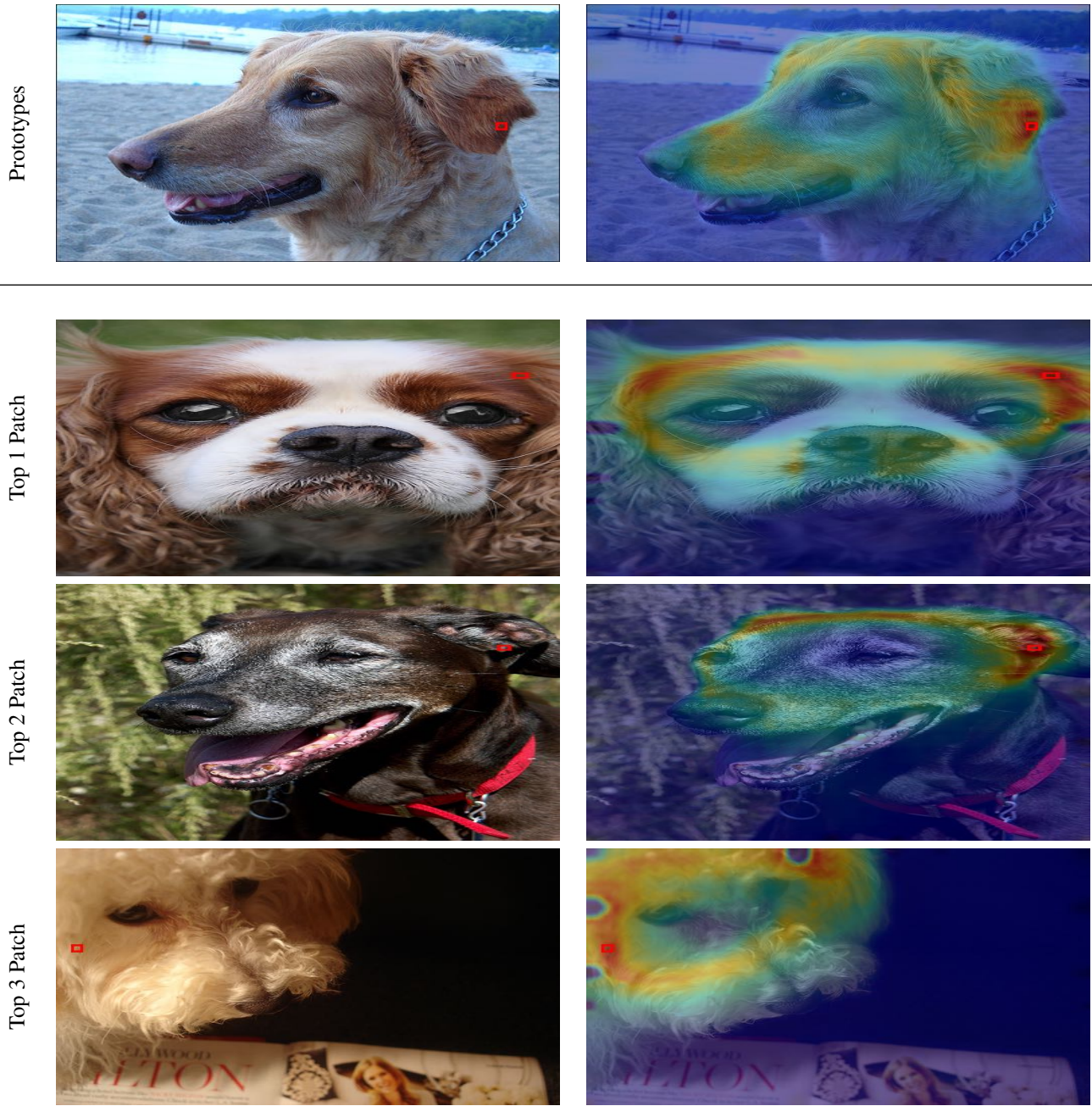


Figure 19. The first row represents a prototype for the class *dog* in PASCAL VOC marked by a red box and the activation of the prototype on its image. The second to fourth rows show the closest patches to the prototype and its activation on the images containing the patches.

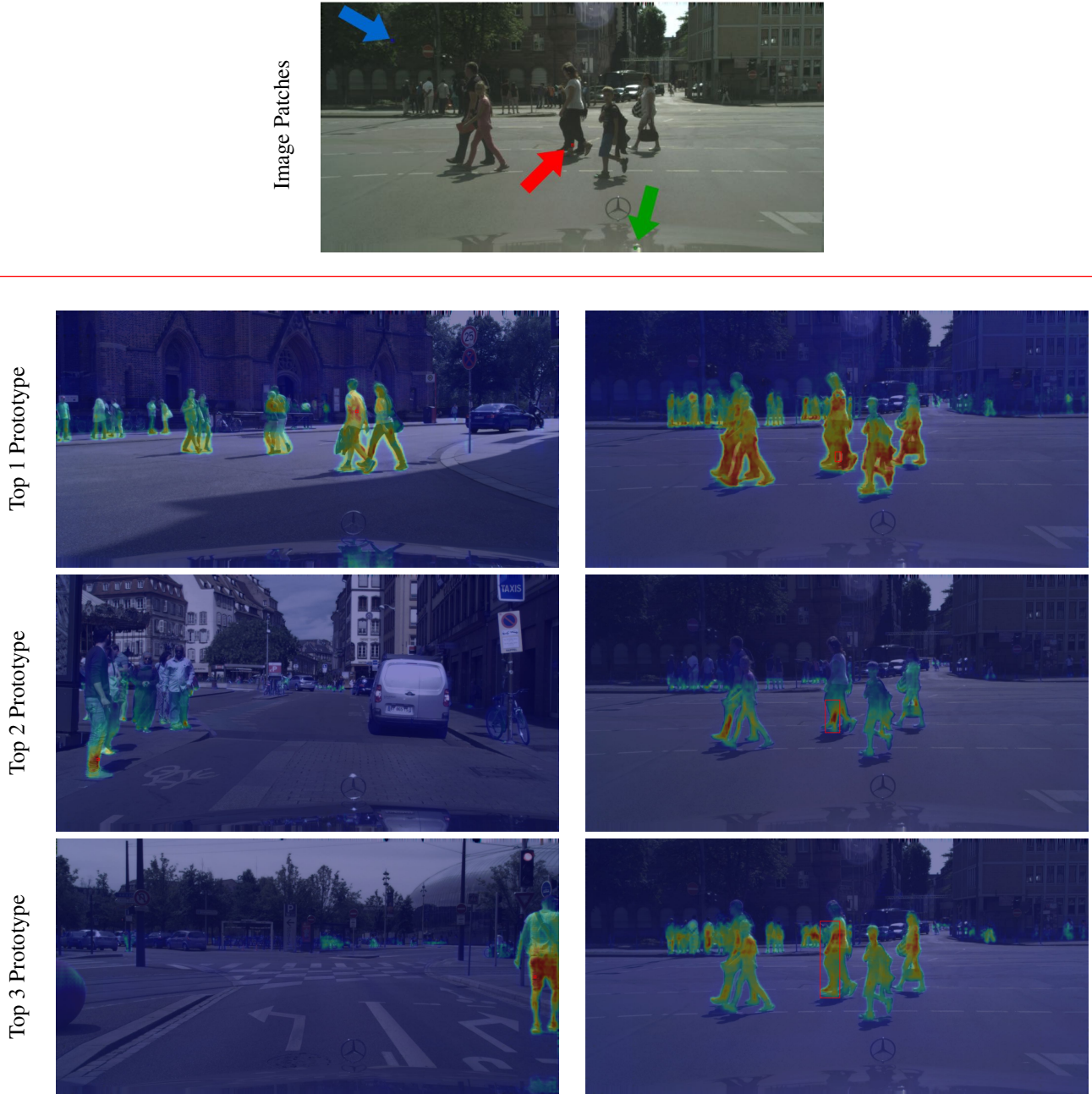


Figure 20. The first row represents a validation image from Cityscapes with three randomly selected patches red, green, blue. The second to fourth rows show the closest prototypes to the red patch via its activation on itself and on the image containing the red patch. In the second column, the bounding boxes correspond to the similarly activated area centered around the random patch.



Figure 21. The first row represents a validation image from Cityscapes with three randomly selected patches red, green, blue. The second to fourth rows show the closest prototypes to the green patch via its activation on itself and on the image containing the green patch. In the second column, the bounding boxes correspond to the similarly activated area centered around the random patch.

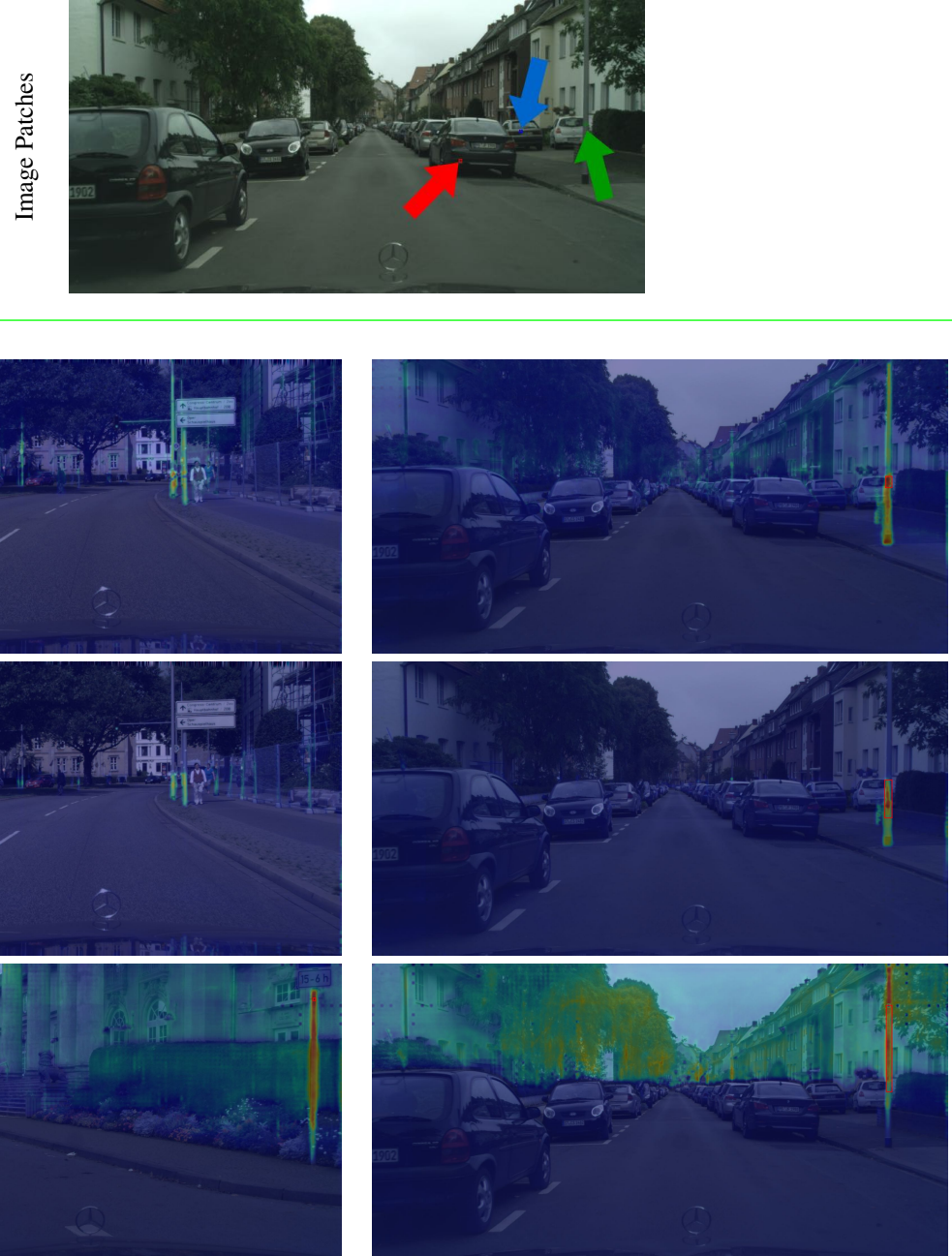


Figure 22. The first row represents a validation image from Cityscapes with three randomly selected patches red, green, blue. The second to fourth rows show the closest prototypes to the green patch via its activation on itself and on the image containing the green patch. In the second column, the bounding boxes correspond to the similarly activated area centered around the random patch.

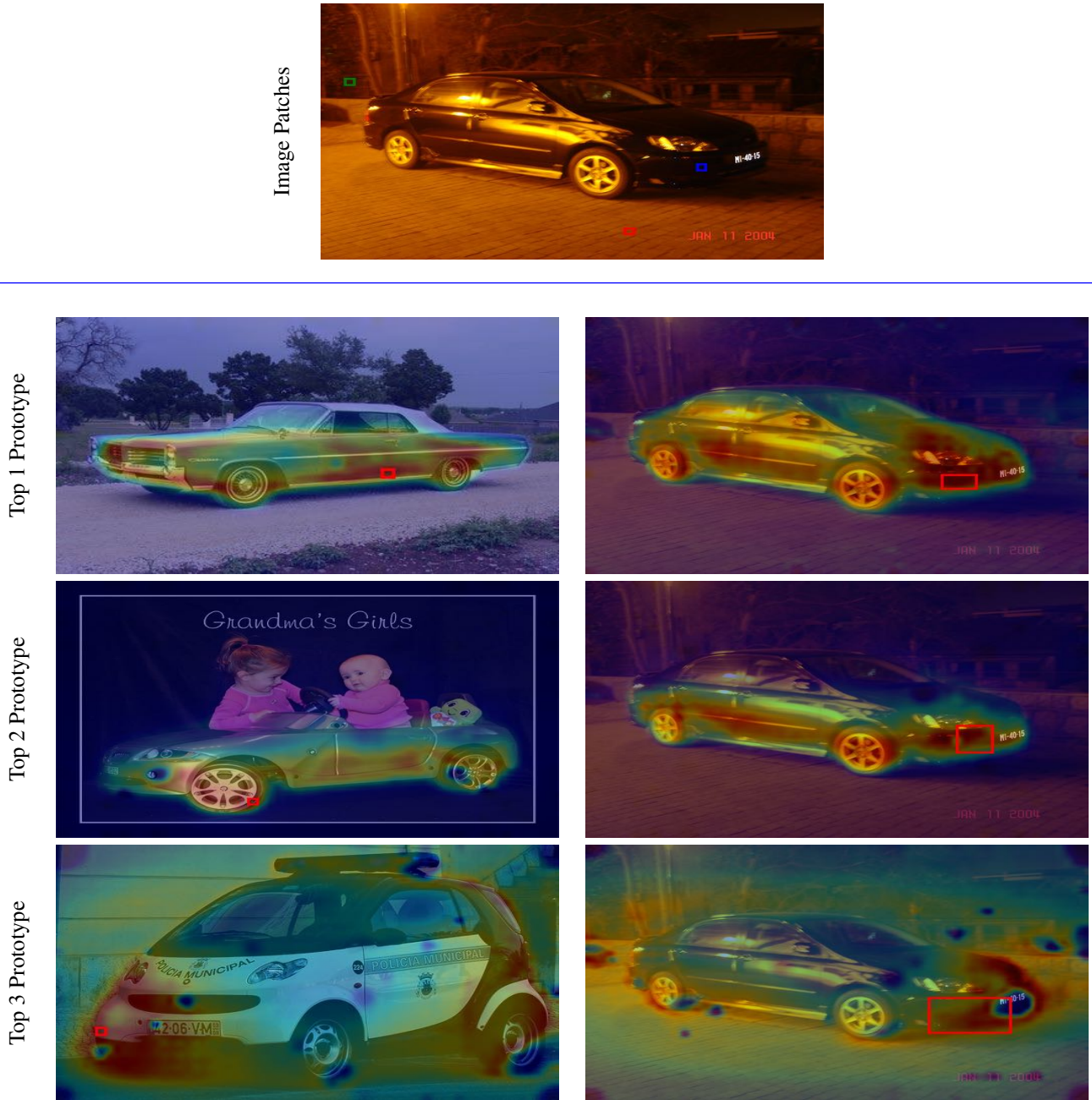


Figure 23. The first row represents a validation image from PASCAL VOC with three randomly selected patches red, green, blue. The second to fourth rows show the closest prototypes to the blue patch via its activation on itself and on the image containing the blue patch. In the second column, the bounding boxes correspond to the similarly activated area centered around the random patch.

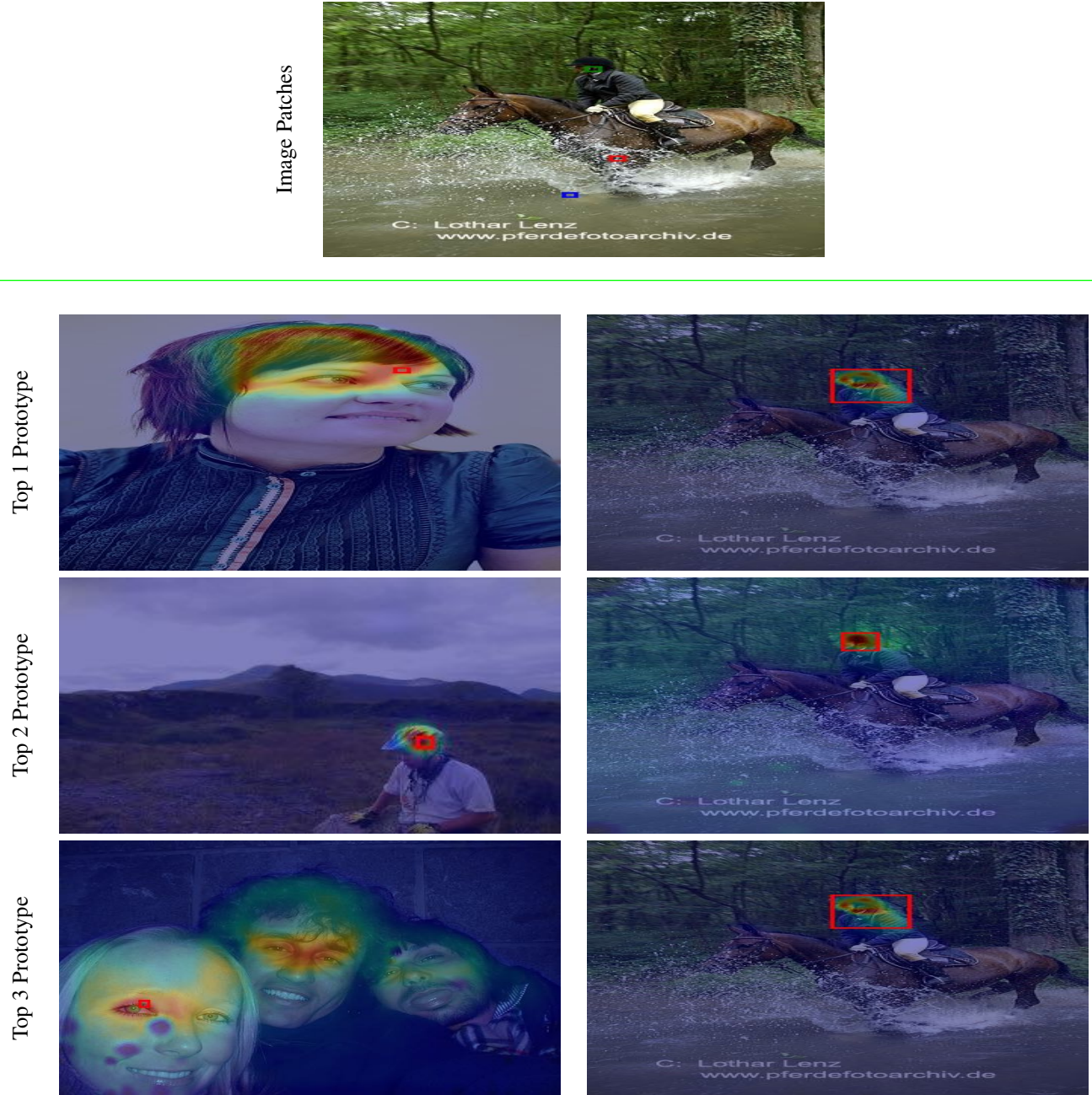


Figure 24. The first row represents a validation image from PASCAL VOC with three randomly selected patches red, green, blue. The second to fourth rows show the closest prototypes to the green patch via its activation on itself and on the image containing the green patch. In the second column, the bounding boxes correspond to the similarly activated area centered around the random patch.

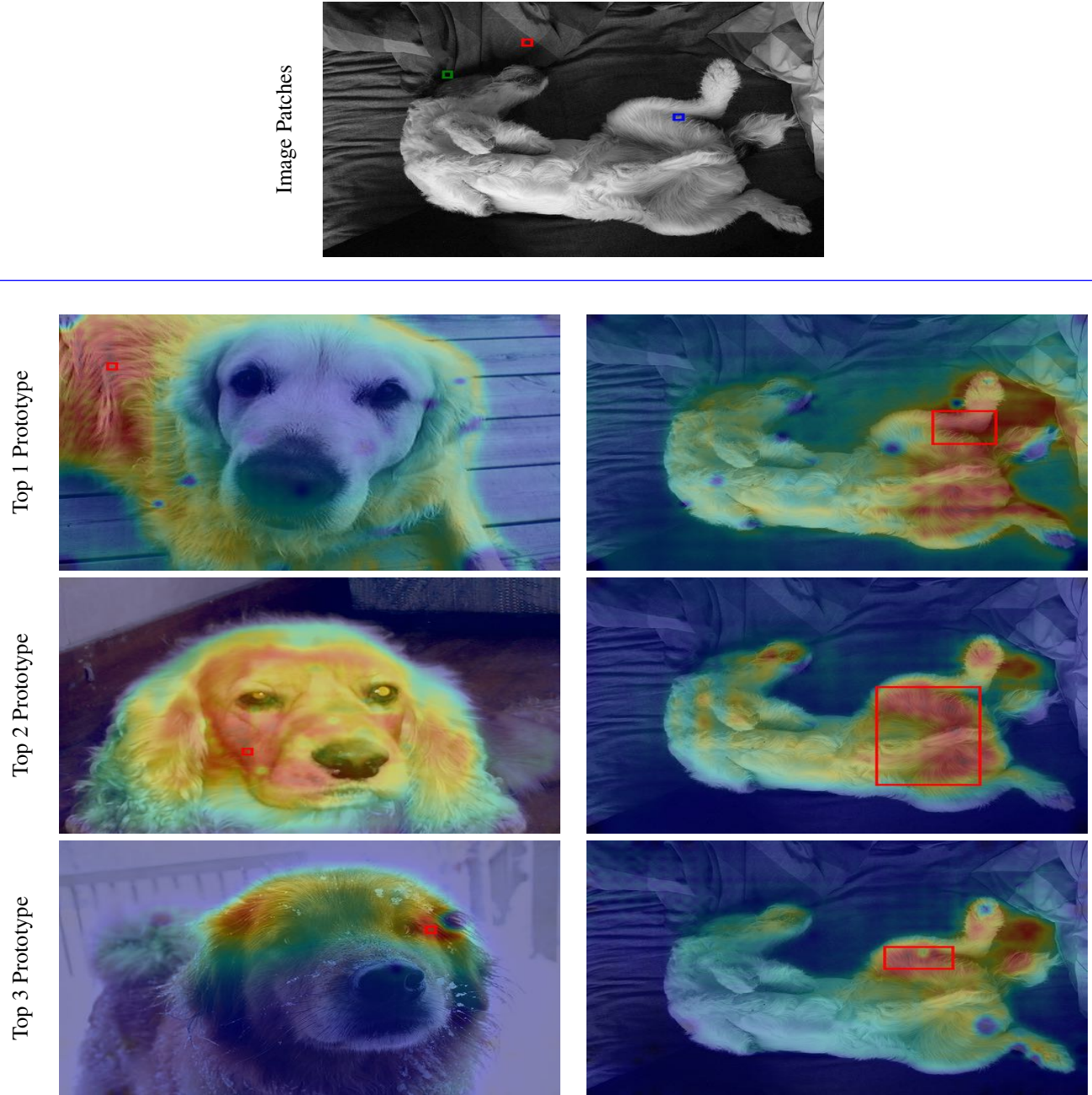


Figure 25. The first row represents a validation image from PASCAL VOC with three randomly selected patches red, green, blue. The second to fourth rows show the closest prototypes to the blue patch via its activation on itself and on the image containing the blue patch. In the second column, the bounding boxes correspond to the similarly activated area centered around the random patch.

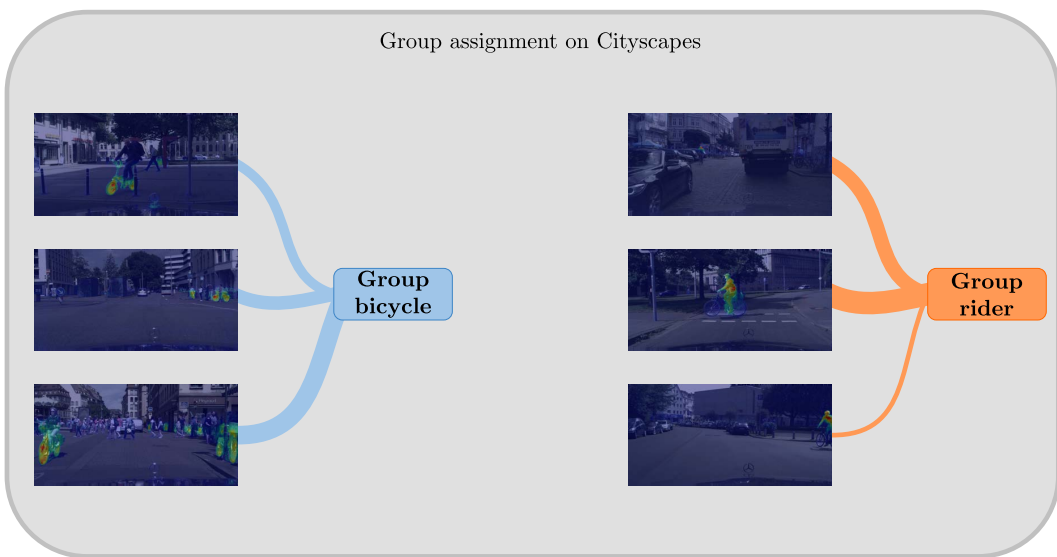
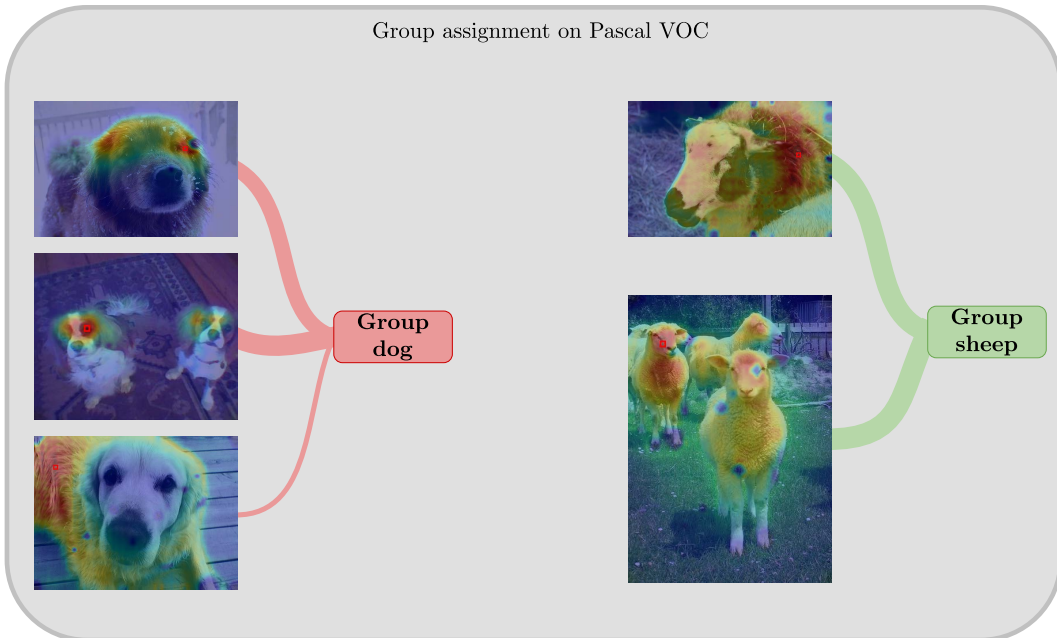


Figure 26. **Top:** for the classes *dog* and *sheep* on Pascal VOC, prototypes with the highest activation for the considered group represent the head. **Bottom:** for the class *bicycle* of Cityscapes, prototypes with the highest activation for the considered group represent the bicycle wheels, while for the class *rider* they mainly highlight the person's upper body.



Figure 27. PASCAL VOC image with its predictions for the class *cow* and in particular the most common error for this class is with the class *sheep*.



Figure 28. Group activations of the class *cow* for the image.



Figure 29. Group activations of the class *sheep* for the image.



Figure 30. Most activated prototypes represented by their training sample and their activation on the input image for Group 1 of class *cow*.

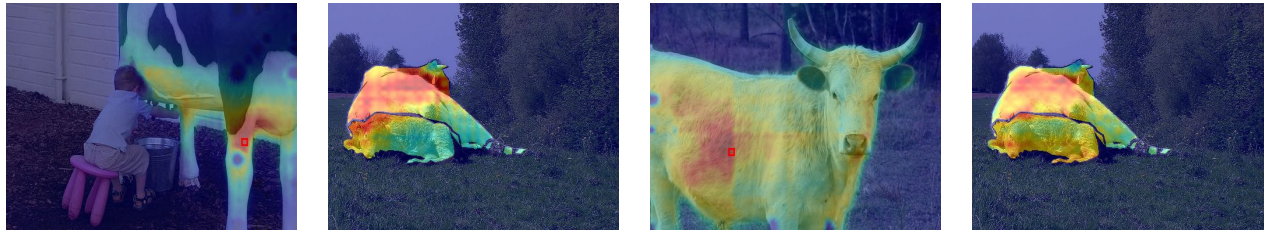


Figure 31. Most activated prototypes represented by their training sample and their activation on the input image for Group 2 of class *cow*.

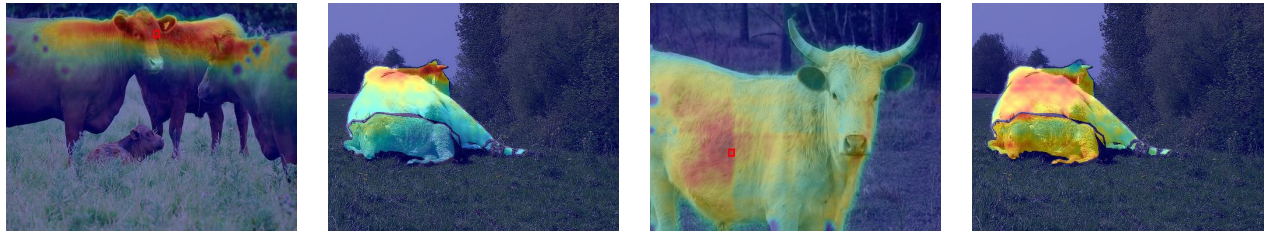


Figure 32. Most activated prototypes represented by their training sample and their activation on the input image for Group 3 of class *cow*.



Figure 33. Most activated prototypes represented by their training sample and their activation on the input image for Group 1 of class *sheep*.



Figure 34. Most activated prototypes represented by their training sample and their activation on the input image for Group 2 of class *sheep*.



Figure 35. Most activated prototypes represented by their training sample and their activation on the input image for Group 3 of class *sheep*.